Acta Neuropathologica (2019) 138:123–145
https://doi.org/10.1007/s00401-019-01988-z

ORIGINAL PAPER

Mitochondrial defect in muscle precedes neuromuscular junction degeneration and motor neuron death in *CHCHD10*$^{S59L/+}$ mouse

Emmanuelle C. Genin[1] · Blandine Madji Hounoum[2] · Sylvie Bannwarth[1] · Konstantina Fragaki[1] · Sandra Lacas-Gervais[3] · Alessandra Mauri-Crouzet[1] · Françoise Lespinasse[1] · Julien Neveu[1] · Baptiste Ropert[1] · Gaelle Augé[1] · Charlotte Cochaud[1] · Cynthia Lefebvre-Omar[4] · Stéphanie Bigou[4] · Aude Chiot[4] · Fanny Mochel[4,5] · Séverine Boillée[4] · Christian S. Lobsiger[4] · Delphine Bohl[4] · Jean-Ehrland Ricci[2] · Véronique Paquis-Flucklinger[1]

Received: 14 December 2018 / Revised: 21 February 2019 / Accepted: 8 March 2019 / Published online: 14 March 2019

Abstract

Recently, we provided genetic basis showing that mitochondrial dysfunction can trigger motor neuron degeneration, through identification of *CHCHD10* encoding a mitochondrial protein. We reported patients, carrying the p.Ser59Leu heterozygous mutation in *CHCHD10*, from a large family with a mitochondrial myopathy associated with motor neuron disease (MND). Rapidly, our group and others reported *CHCHD10* mutations in amyotrophic lateral sclerosis (ALS), frontotemporal dementia-ALS and other neurodegenerative diseases. Here, we generated knock-in (KI) mice, carrying the p.Ser59Leu mutation, that mimic the mitochondrial myopathy with mtDNA instability displayed by the patients from our original family. Before 14 months of age, all KI mice developed a fatal mitochondrial cardiomyopathy associated with enhanced mitophagy. *CHCHD10*$^{S59L/+}$ mice also displayed neuromuscular junction (NMJ) and motor neuron degeneration with hyper-fragmentation of the motor end plate and moderate but significant motor neuron loss in lumbar spinal cord at the end stage of the disease. At this stage, we observed TDP-43 cytoplasmic aggregates in spinal neurons. We also showed that motor neurons differentiated from human iPSC carrying the p.Ser59Leu mutation were much more sensitive to Staurosporine or glutamate-induced caspase activation than control cells. These data confirm that mitochondrial deficiency associated with *CHCHD10* mutations can be at the origin of MND. CHCHD10 is highly expressed in the NMJ post-synaptic part. Importantly, the fragmentation of the motor end plate was associated with abnormal CHCHD10 expression that was also observed closed to NMJs which were morphologically normal. Furthermore, we found OXPHOS deficiency in muscle of *CHCHD10*$^{S59L/+}$ mice at 3 months of age in the absence of neuron loss in spinal cord. Our data show that the pathological effects of the p.Ser59Leu mutation target muscle prior to NMJ and motor neurons. They likely lead to OXPHOS deficiency, loss of cristae junctions and destabilization of internal membrane structure within mitochondria at motor end plate of NMJ, impairing neurotransmission. These data are in favor with a key role for muscle in MND associated with *CHCHD10* mutations.

Keywords CHCHD10 · Mitochondrial disorder · ALS · Mouse model · iPSC

Introduction

Mitochondrial diseases have a large clinical spectrum [16]. However, pure motor neuron disorders are rarely seen in these pathologies. Interestingly, we identified a heterozygous mutation (p.Ser59Leu) in the gene encoding Coiled-Coil-Helix-Coiled-Coil-Helix Domain Containing 10 (*CHCHD10*) in two families. In the first one, patients developed a mitochondrial myopathy with mtDNA deletions and other symptoms including motor neuron disease (MND), cognitive decline resembling frontotemporal dementia (FTD) and cerebellar ataxia [2]. In the second

Emmanuelle C. Genin and Blandine Madji Hounoum contributed equally to this work.

Jean-Ehrland Ricci and Véronique Paquis-Flucklinger contributed as co-last authors.

Electronic supplementary material The online version of this article (https://doi.org/10.1007/s00401-019-01988-z) contains supplementary material, which is available to authorized users.

✉ Véronique Paquis-Flucklinger
paquis@unice.fr

Extended author information available on the last page of the article

family, patients also carried the p.Ser59Leu variant but presented with a typical FTD–amyotrophic lateral sclerosis (FTD–ALS) based on international diagnosis criteria [2]. Among all factors involved in motor neuron degeneration, mitochondrial dysfunction has always been recognized as a major player [7, 37]. However, the identification of *CHCHD10* was the first genetic evidence demonstrating that mitochondria can trigger MND. Mutations in *CHCHD10* were then associated with other diseases, including ALS [20, 26, 34], late-onset spinal motor neuropathy (SMAJ) [30] and Charcot–Marie–Tooth disease type 2 (CMT2) [1].

CHCHD10 is a mitochondrial protein located in the intermembrane space and enriched at cristae junctions [2]. It contains a twin CX_9C domain, which mediates its mitochondrial import through the Mia40-Erv1 disulfide relay system [18, 22]. However, the function of CHCHD10 remains largely unknown despite several studies suggesting an involvement in mitochondrial cristae maintenance [14, 15] and in TDP-43 (TAR DNA-binding protein 43) metabolism [44].

To better understand the biological role of CHCHD10 and to investigate the mechanisms by which mitochondrial dysfunction associated with *CHCHD10* mutations leads to neurodegeneration, we generated knock-in (KI) mice and human induced Pluripotent Stem Cells (iPSC) carrying the heterozygous p.Ser59Leu mutation.

Materials and methods

Generation of the *CHCHD10$^{S59L/+}$* mice

CHCHD10^{S59L} KI mice were generated at Inserm service Unit CIPHE-Phenomin (France) to replace the serine at position 55 by a leucine in the mouse Chchd10 protein. The p.Ser55Leu variation in the mouse protein corresponds to the p.Ser59Leu variant in human CHCHD10 that is responsible for an FTD–ALS phenotype [2] and the KI mice were defined *CHCHD10$^{S59L/+}$* according to the human mutation. The base 'C' at *Chchd10* cDNA position 164 (exon 3) was mutated to a 'T' leading to change in the codon at position 55 from TCA (Ser) to TTA (Leu) in the targeting construct. A floxed neomycin (neo) selectable cassette was placed in intron 3 (100 bp after end of exon 3) and regions of 5′ homology (3.3 kb) and 3′ homology (2.8 kb) were used to drive homologous recombination in C57BL/6N embryonic stem (ES) cells. Following electroporation of the targeting construct, cells were selected for neo resistance. Targeted ES cells were confirmed by Southern blotting. Euploid, targeted ES cells were then microinjected into Balb/cJ blastocysts and re-implanted into pseudopregnant females. Resultant chimeras were bred to C57BL/6N breeders to establish transmission. Germline transmission led to the self-excision of the loxP-Cre-NeoR-loxP cassette in male germinal cells. Routine genotyping was performed by a PCR-based strategy utilizing primers that cover the mutation and remaining the loxP sequence following cre-excision of the selection cassette. The primers were: (forward) 5′GGGTCTTATGGC TCAGATGG′3, (reverse) 5′GGTTAGGACCCTCAAAAT CC′3 and yielded a 268 bp band in wild-type and an additional 353 bp band in *CHCHD10$^{S59L/+}$* mice.

Ethics statement and phenotyping studies

All animal procedures were approved by the Institutional Animal Care and Use Committee at the University of Nice-Sophia Antipolis (Nice, France) and by the Ministère de l'Education Nationale, de l'Enseignement Supérieur et de la Recherche (MESR agreement: APAFIS#5870-2016061017306888). Weights of the *CHCHD10$^{S59L/+}$* and wild-type (WT) animals were measured on a weekly basis to follow body mass development. Food intake and some of phenotypic parameters including sensory–motor functions (Rotarod, grip and string tests, crenelated beam), echocardiography, electrocardiography, weight of mouse organs and blood lactate were analyzed at Phenomin-ICS, Illkirch, France. For these studies, the population included 40 C57BL/6N mice (20 males and 20 females), divided into 2 groups (10 *CHCHD10$^{S59L/+}$* and 10 *CHCHD10$^{+/+}$* of each sex). All animal procedures and experiments were approved by the local ethical committee (Comité d'Ethique en Expérimentation Animale IGBMC-ICS) for Animal Care and Use and MESR.

Muscle/heart histopathology and ultrastructure

Muscle and heart samples were, respectively, frozen in cooled isopentane and liquid nitrogen for histological and histoenzymatic analysis including Gomori-modified trichrome staining, cytochrome *c* oxidase (COX) activity, succinate dehydrogenase (SDH) activity and double COX/SDH staining according to the standard protocols. For electron microscopy, mice were treated with buprecare (0.1 mg/kg) and deeply anesthetized with dolethal (50 mg/kg). Then, they were transcardially perfused with 0.9% NaCl, followed by 2.5% Glutaraldehyde (GA). Gastrocnemius muscle, lumbar spinal cord, brain and heart were post-fixed in 2.5% GA. After an adequate fixation, the samples were rinsed in 0.1 M cacodylate buffer, and post-fixed for 2 h in 1% osmium tetroxide and 1% potassium ferrocyanide in 0.1 M cacodylate buffer to enhance the staining of membranes. Samples were then rinsed in distilled water, dehydrated in alcohols and lastly embedded in epoxy resin. The heart samples were dehydrated and embedded with an automat Leica EM AMW. Contrasted ultrathin sections (70 nm) were analyzed under a JEOL 1400 transmission electron microscope mounted with a Morada Olympus CCD camera.

RNA isolation and quantitative real-time PCR

The total RNA from tissues was extracted using TRIzol reagent (ThermoFisher Scientific). Prior to reverse transcription, residual genomic DNA was removed from total RNA with DNase I (ThermoFisher Scientific). cDNA was then reverse-transcribed using transcription first strand cDNA synthesis kit (Roche Applied Science) with 1 µg total RNA and oligo-dT as primer. All PCRs were performed in triplicate. Quantitative RT-PCR was carried out using SYBR Green master mix (Roche Applied Science) on a Light Cycler LC480. Results were normalized to OAZ1 or HPRT. Primer sequences have previously been described [3].

Western blotting

The concentration of proteins was determined using the Pierce BCA assay kit (Thermo Fisher Scientific). 2.5–20 µg of total protein extracts were separated on acrylamide-SDS gels and transferred to PVDF membranes (Millipore). Specific proteins were detected using different antibodies listed in suppl. Table 1 (Online Resource 8). Signals were detected using a chemiluminescence system (Immobilon Western HRP Chemilumiscent substrates, Millipore). ImageJ was used to quantify protein signals.

Oxidative phosphorylation spectrophotometric measurements

Enzymatic spectrophotometric measurements of the oxidative phosphorylation respiratory chain complexes and citrate synthase were performed at 37 °C on crude tissue homogenates according to the standard procedures [35]. Proteins were measured according to Bradford microassay [6] and results were expressed as nmol/min/mg of proteins.

Mitochondrial DNA molecular analysis

Total DNA was extracted using standard phenol/chloroform procedure. Long-range PCR and Southern blot analysis were performed as previously described [3]. Mitochondrial DNA quantification was performed by real-time quantitative PCR as previously described [3]. Primer sequences and PCR conditions are available on request.

Blood lactate

Blood was collected by retro-orbital puncture under isoflurane anesthesia at 12.00 am on mice fasted for 4 h. Blood lactate was measured on a drop of total blood using blood lactate monitor and lactate test strips (Roche Diagnostics, Accutrend).

Analysis of neuromuscular junctions (NMJs)

Mice were treated with buprecare (0.1 mg/kg) and deeply anesthetized with dolethal (50 mg/kg). Then, they were transcardially perfused with 0.9% NaCl, followed by 4% paraformaldehyde (PFA). Gastrocnemius muscles were post-fixed in 4% PFA for 4 h and then cryoprotected in 20% sucrose for 24 h. Samples were snap-frozen in isopentane after cryoprotection with Cryomatrix (Thermo Scientific). For gastrocnemius muscle, 40-µm-thick free-floating serial sections were longitudinally sliced using cryostat. For immunostaining, muscle sections were incubated in blocking buffer (0.5% Triton X-100, 5% normal goat serum, 4% bovine serum albumin (BSA)) for 4 h at RT. Floating sections were stained with primary antibodies diluted in blocking buffer for 3 days, at 4 °C. The following primary antibodies were used: neurofilament (NF-M), synaptophysin (Syn), CHCHD10 and TOM20. The references of antibodies and the concentrations used are listed in suppl. Table 1 (Online Resource 8). After several washings in PBS/Triton 0.1%, muscle sections were incubated for 1.5 h, at RT, in a solution (PBS/Triton 0.3%) containing the α-Bungarotoxin (BTX) coupled to Alexa Fluor 488 and with the corresponding secondary antibody for NF-M, Syn, TOM20 or CHCHD10 [listed in suppl. Table 1 (Online Resource 8)]. Finally, muscle sections were rinsed in PBS/Triton 0.1% and PBS, and mounted in Fluoromount-G mounting medium (SouthernBiotech). All images were captured with a ZEISS LSM 880 confocal laser-scanning microscope. *Z*-stacked confocal images were done to capture the entire NMJ. Confocal settings were optimized to achieve the best compromise between image quality and acquisition rate: 8 bit depth, 512 × 512 frame size, 63× magnification, 2× zoom, average of 2 and 0.6 µm *z*-stack intervals. Six mice per genotype were analyzed and 20–25 NMJs per animal were randomly chosen and analyzed with NMJ-morph method (NIH-Imaje/Imaje/J), leading to measure 21 separate pre-and post-synaptic variables (as described in Jones et al. [21]).

Motor neurons count and TDP-43 expression in lumbar spinal cord

Lumbar spinal cords were collected and frozen as described previously for gastrocnemius muscle samples. Thirty-micrometer serial lumbar spinal cord cryosections were cut using cryostat. A total of seven mice per genotype at end stage and four mice per genotype at 3 months of age were quantified. Seventeen to 20 lumbar (L3–L6) sections per animal were stained with cresyl-violet-acetate (Sigma). All the motor neurons (diameter > 25 µm) in the ventral horn were

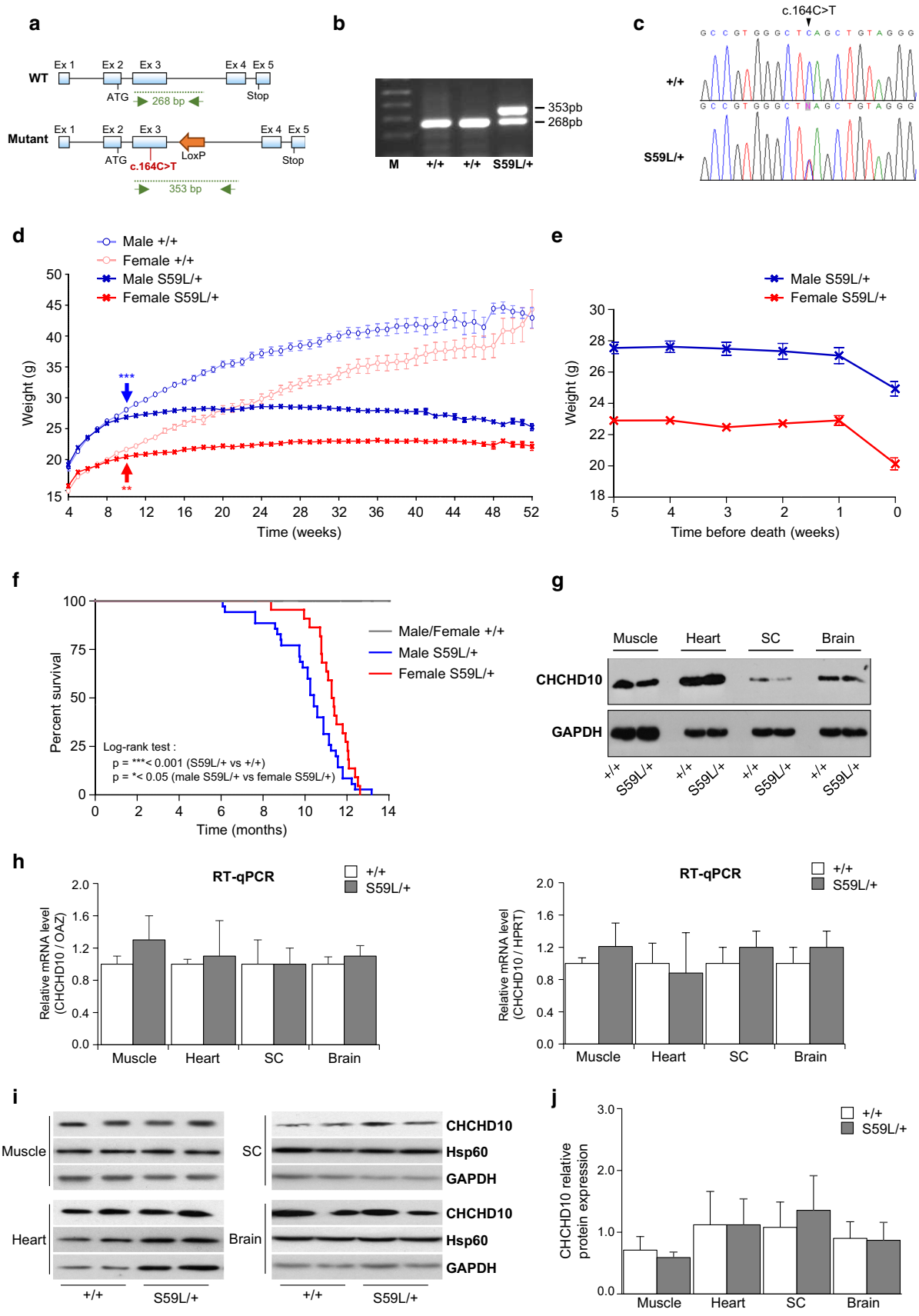
a
WT
Ex 1
Ex 2
Ex 3
Ex 4
Ex 5
ATG
268 bp
Stop
Mutant
LoxP
c.164C>T
353 bp
b
353pb
268pb
M
+/+
+/+
S59L/+
c
c.164C>T
+/+
S59L/+
d
Male +/+
Female +/+
Male S59L/+
Female S59L/+
Weight (g)
Time (weeks)
e
Male S59L/+
Female S59L/+
Weight (g)
Time before death (weeks)
f
Male/Female +/+
Male S59L/+
Female S59L/+
Percent survival
Log-rank test :
p = ***< 0.001 (S59L/+ vs +/+)
p = *< 0.05 (male S59L/+ vs female S59L/+)
Time (months)
g
Muscle
Heart
SC
Brain
CHCHD10
GAPDH
+/+
S59L/+
h
RT-qPCR
+/+
S59L/+
Relative mRNA level (CHCHD10 / OAZ)
Relative mRNA level (CHCHD10 / HPRT)
Muscle
Heart
SC
Brain
i
Muscle
Heart
SC
Brain
CHCHD10
Hsp60
GAPDH
+/+
S59L/+
j
+/+
S59L/+
CHCHD10 relative protein expression
Muscle
Heart
SC
Brain

◂**Fig. 1** Generation and characterization of *CHCHD10*$^{S59L/+}$ mice. **a** Drawing of the wild-type (+/+) allele (top) and the *CHCHD10*^{S59L} allele (below). The alleles depict the localization of exons 1–5, the residual Lox P site and the position of the mutation c.164C > T. The primers used for genotyping are indicated by arrows. **b** PCR genotyping strategy showing the wild-type (268 bp) and the mutated (353 bp) amplicons. *M* molecular weight marker. **c** Sequencing of cDNA showing the presence of the heterozygous c.164C > T mutation at the RNA level in the *CHCHD10*$^{S59L/+}$ mouse. **d** Body weight curves showing failure to gain weight from 10 weeks of age (arrows) for both male and female S59L/+ mice that were significantly leaner than their littermates. Shown are mean ± SEM (n = 52–59 mice per gender and genotype at 10 weeks of age). Statistical analysis was performed using one-way ANOVA followed by Bonferroni's post hoc comparison tests. P value = **< 0.01, ***< 0.001. **e** Body weight curves during the last 5 weeks of life showing the speed of weight loss before the end stage, leading to mouse euthanasia. **f** Survival curve of the *CHCHD10*$^{S59L/+}$ mice (n = 35 male and 22 female S59L/+ mice). Survival analysis was conducted using the Log-rank (Mantel-Cox) test. P value = ***< 0.001 (S59L/+ versus +/+ mice) and *< 0.05 (male S59L/+ versus female S59L/+ mice). **g** Western blot analysis from equal amounts (20 µg) of muscle, heart, lumbar spinal cord (SC) and brain (cortex/hippocampus) homogenates of +/+ and S59L/+ mice revealed with CHCHD10 and GAPDH (loading control) antibodies. **h** Quantitative RT-PCR analysis for *CHCHD10* mRNA expression in skeletal muscle, heart, lumbar spinal cord and brain (cortex/hippocampus). *CHCHD10* expression levels were quantified as the ratio to *OAZ* (left) or to *HPRT* (right) and the values of *CHCHD10/OAZ* or *CHCHD10/HPRT* were normalized to that of control. Data are shown as the mean ± SD of 3 independent experiments (n = 3 +/+ and 3 S59L/+ mice). **i** Representative western blot analysis of muscle (30 µg), heart (20 µg), lumbar spinal cord (SC) (100 µg) and brain (cortex/hippocampus) (100 µg) homogenates from +/+ and S59L/+ mice, at 3 months of age, using CHCHD10, Hsp60 and GAPDH (loading control) antibodies. **j** Quantification of relative intensities of proteins shown in **i**. Data are shown as the mean ± SD of 2–3 independent experiments (n = 2 +/+ and 2 S59L/+ mice). In **h** and **j**, the data from S59L/+ mice were compared to the controls using Mann–Whitney's test

counted bilaterally and averaged per lumbar section. Motor neuron quantifications were performed by two experimenters blind to the experimental conditions.

For immunostaining with TDP-43 and Tuj1 antibodies, lumbar sections were incubated with antigen retrieval for 15 min at 95 °C [Citrate buffer (pH 6), Target Retrieval Solution, Dako] and then in blocking buffer [0.25% Triton X-100, 5% normal goat serum, 2% bovine serum albumin (BSA)] for 1 h at RT. Floating sections were stained with primary antibodies diluted in blocking buffer O/N, at 4 °C. The references of antibodies and the concentrations used are listed in suppl. Table 1 (Online Resource 8). After several washings in PBS/Triton 0.1%, lumbar sections were incubated for 2 h, at RT, in a solution containing 0.25% Triton X-100, 1% BSA and with the corresponding secondary antibody [listed in suppl. Table 1 (Online Resource 8)]. Finally, lumbar sections were rinsed in PBS/Triton 0.1% and PBS, and mounted in Fluoromount-G mounting medium (SouthernBiotech). All images were captured with a ZEISS LSM 880 confocal laser-scanning microscope. Three mice per genotype were analyzed with 5–7 lumbar sections randomly chosen and analyzed per animal.

Rotarod test

This test measures the ability of an animal to maintain balance on a rotating rod (Bioseb, Chaville, France). Mice were given three testing trials during which the rotation speed accelerated from 4 to 40 rpm in 5 min. Trials were separated by 5–10 min interval. The average latency was used as index of motor coordination performance.

Grip test

This test measures the maximal muscle strength (g) using an isometric dynamometer connected to a grid (Bioseb). Mice were allowed to grip the grid with all their paws, then they were pulled backwards until they released it. Each mouse was submitted to three consecutive trials. The maximal strength developed by the mouse before releasing the grid was recorded and the result corresponds to the average value of the three trials.

String test

The apparatus is a wire stretched horizontally 40 cm above the bench. Testing consisted of three trials separated by 5–10 min interval. On each trial, the forepaws of the animal were placed on the thread. The latency the animal took to catch the wire with its hindpaws was recorded.

Crenelated beam

This test allows gait analysis which is relatively specific for evaluation of proprioceptive sensitivity. The performance in this test depends also on the integrity of motor coordination and vestibular function. Animals require an accurate paw placement to succeed in this test. The gait is altered in ataxia or in case of neuropathic pain for example. The apparatus is a 1.7 cm wide and 63 cm long crenelated wooden beam, elevated 18 cm above the bench surface. Crenels are 2 cm long and 2 cm deep. The two extremities of the beam are not crenelated and used as starting and goal points during testing. A home is placed at the goal point to allow mice being motivated to perform the task. Animals were submitted to three testing trials during which they were placed at the starting extremity and allowed to walk the beam distance. The latency to cross the beam and the number of hind paws fails (when one or both hind paws misses the merlon and slip in the crenellated parts of the beam) were measured.

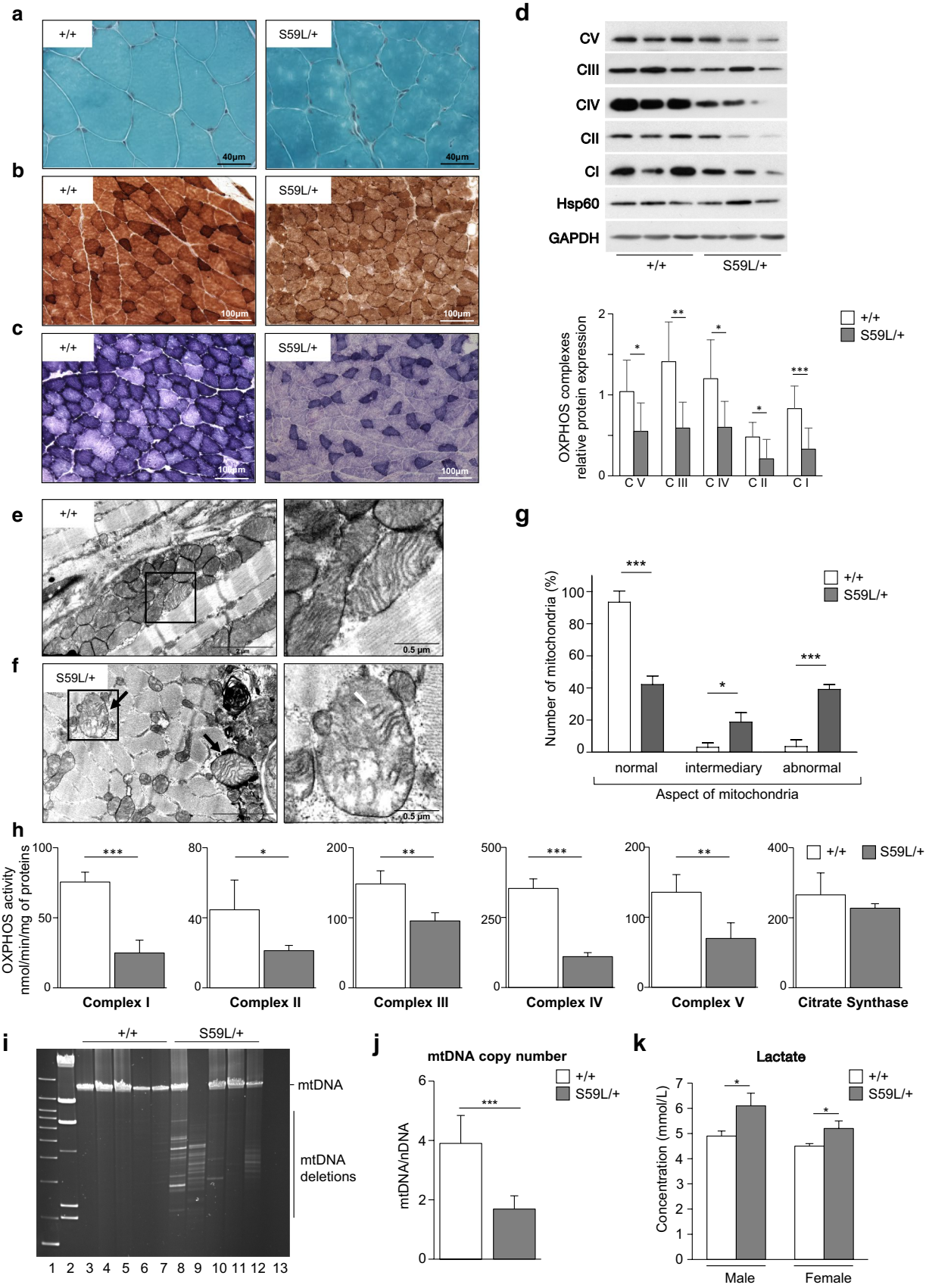
a
+/+
S59L/+
40µm
b
100µm
c
d
CV
CIII
CIV
CII
CI
Hsp60
GAPDH
OXPHOS complexes relative protein expression
C V
C III
C IV
C II
C I
e
0.5 µm
f
g
Number of mitochondria (%)
normal
intermediary
abnormal
Aspect of mitochondria
h
OXPHOS activity nmol/min/mg of proteins
Complex I
Complex II
Complex III
Complex IV
Complex V
Citrate Synthase
i
mtDNA
mtDNA deletions
1 2 3 4 5 6 7 8 9 10 11 12 13
j
mtDNA copy number
mtDNA/nDNA
k
Lactate
Concentration (mmol/L)
Male
Female

◂**Fig. 2** Muscle analysis of *CHCHD10*$^{S59L/+}$ mice at the end stage. Histopathology of muscle from +/+ (left panels) and S59L/+ (right panels) mice with Gomori-modified trichrome (**a**), COX-SDH stain (**b**) and SDH stain (**c**). Scale bars: 40 µm in **a** and 100 µm in **b**, **c**. **d** Representative western blot analysis (upper panel) from equal amounts (2.5 µg) of muscle homogenates of +/+ and S59L/+ mice using OXPHOS antibodies cocktail detecting NDUFB8 (complex I), SDHB (complex II), UQCRC2 (complex III), MT-CO1 (complex IV), ATP5A (complex V), anti-Hsp60 and anti-GAPDH antibody for loading control. Quantification of relative intensities of OXPHOS proteins, related to GAPDH expression, in +/+ (white) and S59L/+ (gray) mice is shown in lower panel. Data are shown as the mean ± SD of 3–4 independent experiments ($n = 3$ +/+ and 3 S59L/+ mice). Ultrastructure of skeletal muscle from +/+ (**e**) and S59L/+ (**f**) mice showing abnormal mitochondria (arrows) in mutant animals. Enlarged mitochondria with abnormal cristae are visible in S59L/+ muscle. The right panel of each image is a magnification of the area indicated by the square in the left panel. Scale bars: 2 µm in left panels and 0.5 µm in right panels. **g** Quantification of mitochondrial morphology observed in **e** and **f**. Intermediary refers to mitochondria that cannot be clearly classified as abnormal despite the presence of slight cristae anomalies. Shown are mean ± SEM ($n = 3$ +/+ and 3 S59L/+ mice with at least 170 mitochondria per animal randomly chosen and analyzed). **h** Spectrophotometric analysis of respiratory chain in muscle from +/+ and S59L/+ mice. Results represent the mean ± SD of 3 +/+ and 3 S59L/+ mice. **i** Long extension PCR of mtDNA from muscle of 5 +/+ (lanes 3–7) and 5 S59L/+ (lanes 8–12) mice. mtDNA indicates the 12.8 kb amplicon. Lanes 1, 2: molecular weight markers. Lane 13: negative PCR control. **j** Mitochondrial DNA quantification in muscle of +/+ and S59L/+ mice. The mouse mitochondrial 12S rRNA (mtDNA) and the nuclear GAPDH (nDNA) genes were individually amplified by real-time PCR. Data were expressed as ratio between mtDNA and nDNA concentration. Results represent the mean of relative PCR ± SD of 3 independent experiments from 5 +/+ and 6 S59L/+ mice. **k** Lactate levels in blood. Data are mean ± SEM of 33-week-old mice ($n = 9$ +/+ mice for each gender, $n = 10$ and 9 for male and female S59L/+ mice, respectively). The data from S59L/+ mice were compared to the controls. Statistical analysis was performed using Mann–Whitney's test in **d**, **j** and **k** and Student's *t* test in **g** and **h**. *P* value = *< 0.05, **< 0.01, ***< 0.001

Electromyography (EMG)

EMG recordings were performed under ketamine–xylazine anesthesia using a Key Point electromyograph apparatus (Medtronic, France). Body temperature was maintained at 37 °C with a homeothermic blanket (Harvard, Paris, France). To measure sensory nerve conduction velocities (SNCV), recording electrodes were inserted at the base of the tail and stimulating electrodes placed 20 mm from the recording needles towards the extremity of the tail. A ground needle electrode was inserted between the stimulating and recording needles. Caudal nerve was stimulated with a series of 20 pulses during 0.2 ms each at a supramaximal intensity. The mean response of these 20 stimulations was used for statistical analysis. Compound muscle action potentials (CMAP) were measured in gastrocnemius muscle after stimulation of the sciatic nerve. For this purpose, stimulating electrodes were placed at the level of the sciatic nerve and recording electrodes placed in the gastrocnemius muscle. A ground needle was inserted in the contralateral paw. Sciatic nerve was stimulated with a single 0.2 ms pulse at a supramaximal intensity. The amplitude (mV) and the distal latency (ms) of the responses were measured.

Echocardiography

In brief, mice were anesthetized with inhaled isoflurane (1–2%) and placed on a heated imaging platform. The temperature and heart rate of the mouse were constantly monitored to minimize physiological variation. Mice were imaged using a high-frequency echocardiography machine (Vevo-2100, VisualSonics, Inc., Toronto, Canada) and a standardized protocol was applied to systematically evaluate cardiac size and function. Once completed, the mice were easily woken up after breathing oxygen for a short time and were returned to their cage. Transthoracic echocardiographic images were captured by the mean of a 30 MHz linear probe (MS 400). The following parameters were recorded to assess:

- cardiac morphology and ventricular systolic function (Short axis, SAX): left ventricular end-diastolic (LVEDD) and end-systolic diameters (LVESD), septal wall (SW) and posterior wall thicknesses (PW), left ventricular mass (LVM = 1.055 × [(EDD + SW + PW) 3-EDD3)]), ejection and shortening fraction and cardiac output;
- hemodynamic profiles: aortic artery velocity and pressures to detect intra-cardiac pressures changes.

Electrocardiography (ECG)

We evaluated cardiac electrophysiology in anesthetized mice (isoflurane 1–2%) using an electrocardiograph ISO DAM8 amplifier (World Precision Instruments, USA) and Analogic-numeric conversion box (ITF16A/D converter, EMKA technologies, USA). Surface electrodes were placed in the right arm and the left hind paw (DII configuration). ECG was used to detect a relative conduction system defect by analyzing the rate (RR interval) and regularity of heartbeats, as well as the duration of normal atrial (PR, Pdur…) and ventricular (QRS, ST…) depolarization, ventricular repolarization (QT interval) and the presence of any ischemic heart damage (ST segment).

Preparation of mouse embryonic fibroblasts (MEFs)

Primary +/+ and S59L/+ MEFs were isolated from +/+ and S59L/+ embryos at embryonic day 13 (E13) using standard methods [3]. Briefly, the heads were removed to allow genotyping. Then, freshly dissected mouse embryos were rinsed,

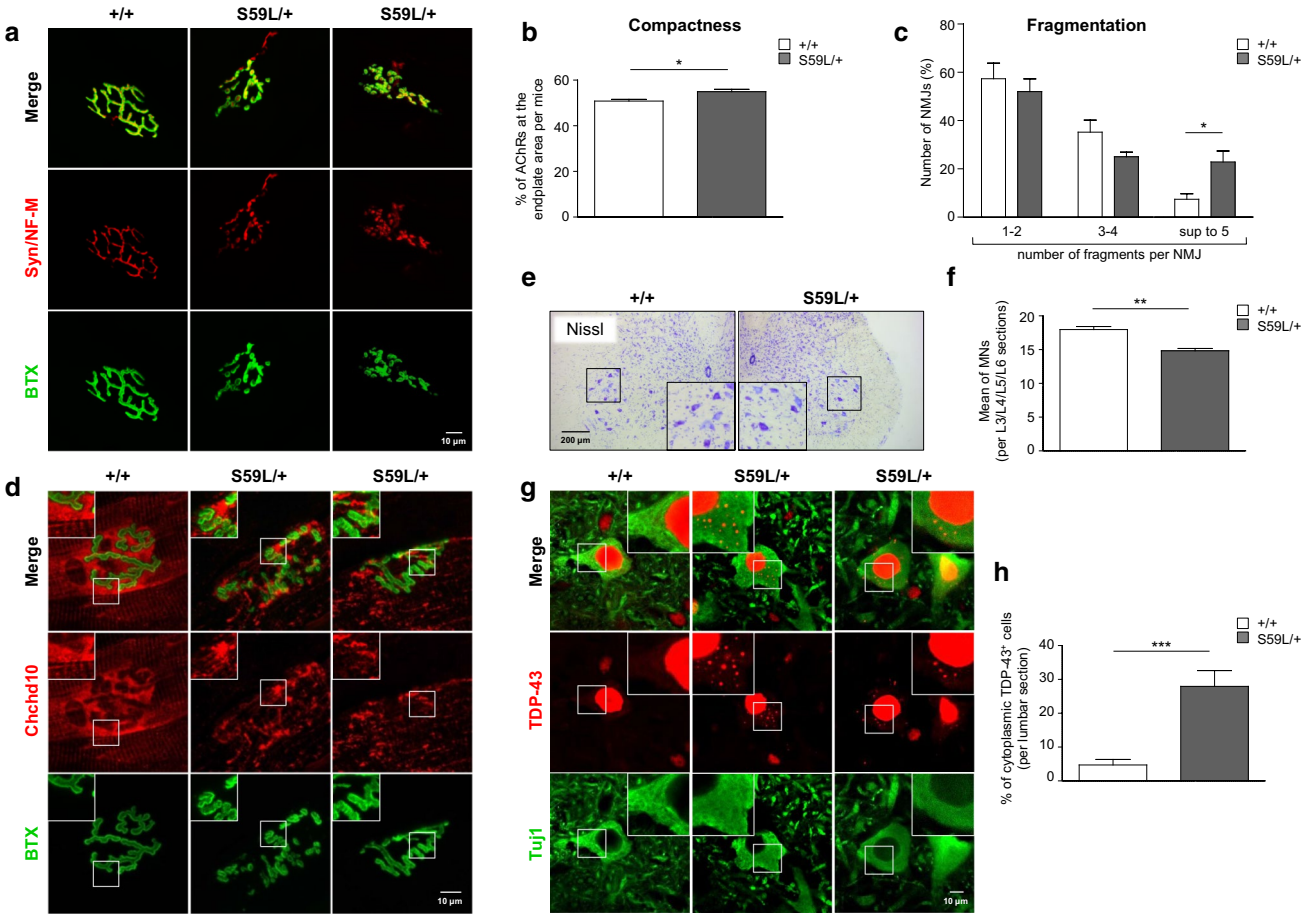

Fig. 3 NMJ fragmentation, motor neuron degeneration and TDP-43 proteinopathy in *CHCHD10*$^{S59L/+}$ mice at end stage. **a** Maximum intensity projection of *Z*-stacked confocal images of NMJs in the gastrocnemius muscle from one +/+ and two S59L/+ mice showing fragmented motor end plate in KI animals. Neurofilament (NF-M, red) and synaptophysin (Syn, red) were used to identify axons and presynaptic terminals. α-Bungarotoxin (BTX, green) was used to identify the post-synaptic domain. Scale bar: 10 µm. **b**, **c** NMJs shown in a were quantified using NMJ-morph method [21]. Shown are mean ± SEM ($n = 6$ +/+ mice and 6 S59L/+ mice with 20 to 25 NMJs per animal randomly chosen and analyzed). **b** Quantitative analysis of the compactness of AChRs at the endplate of NMJ. The compactness corresponds to the quantity of AChRs within a given area and was defined as follows: [AChR area/endplate area] × 100. **c** Quantitative analysis of the fragmentation of NMJs. NMJs were categorized into groups according to their number of fragments. The number of NMJs in each group is given as percentage of total NMJ number for each genotype. **d** CHCHD10 expression around NMJs in the gastrocnemius muscle from one +/+ and two S59L/+ mice. A maximum intensity projection of *Z*-stacked confocal images showed immunofluorescent staining of CHCHD10 (red) and α-Bungarotoxin (BTX, green) to mark NMJ ($n = 3$ +/+ and 3 S59L/+ mice). Scale bar: 10 µm. **e** Nissl staining of lumbar spinal cords from +/+ and S59L/+ mice showing large motor neurons (insets). Scale bar: 200 µm. **f** Quantification of motor neurons in the ventral horns of lumbar spinal cord (between L3 and L6 sections). Shown are mean ± SEM ($n = 7$ +/+ mice and 7 S59L/+ mice). **g** TDP-43 and Tuj1 expression in lumbar spinal neurons from one +/+ and two S59L/+ mice showing cytoplasmic TDP-43 aggregates in mutant animals. **h** Quantification of neurons positive for TDP-43 cytoplasmic aggregates per lumbar section. Shown are mean ± SEM ($n = 3$ +/+ and 3 S59L/+ mice with 5–7 lumbar sections randomly chosen and analyzed per animal). In **b**, **c**, **f** and **h**, the data from S59L/+ mice were compared to the controls using Mann–Whitney's test. *P* value = *< 0.05, **< 0.01, ***< 0.001

incubated with trypsin/EDTA 1X for 5–10 min, and seeded in glucose Dulbecco's modified Eagle's medium (DMEM, Gibco) supplemented with 10% fetal bovine serum (FBS), penicillin (100U/ml)/streptomycin (0.1 mg/ml) and gentamycin (0.6 mg/ml). Cells were grown in DMEM supplemented with 10% FBS and penicillin (100U/ml)/streptomycin (0.1 mg/ml), at 37 °C in a humidified atmosphere with 5% CO_2 in air.

Culture of NSC-34 cells

The NSC-34 cell line (Catalogue number-CLU140) was purchased from Cedarlane Laboratories (via Tebu-Bio, Le Perray en Yvelines, France). Cells were cultured in DMEM with 10% (v:v) heat-inactivated FBS and 1% (v:v) penicillin/streptomycin. Cells were subcultured every 2–3 days. NSC-34 cells were transfected with empty vector (EV) or vectors encoding human wild-type CHCHD10-FLAG

(WT) or mutant CHCHD10-FLAG (S59L) using Lipofectamine™2000 (Invitrogen) and selection was made with 0.5 mg/ml Geneticin (G-418) sulfate.

iPSC generation and characterization

iPSC clones were generated from human fibroblasts with the integration-free CytoTune-iPS 2.0 Sendai Reprogramming Kit (Thermo Fisher Scientific) under feeder-free conditions. The skin fibroblast culture from the control subject (69-year-old woman) was obtained from the Centre de Ressources Biologiques (CRB) (Lyon, France) according to French laws. Skin fibroblasts from one patient carrying the heterozygous p.Ser59Leu variant in *CHCHD10* (58 year-old woman, subject V-10 in Bannwarth et al. [2]) were obtained after informed consent of the patient and validation by the department of personal data protection officer of Nice Teaching Hospital in accordance with the Declaration of Helsinki protocols and act no. 78–17 of 6 January 1978. iPSC clones were individually picked and transferred to Geltrex-coated plates and cultured in Essential 8 Medium (Thermo Fisher Scientific). iPSC clones were fed daily and passaged either manually or with EDTA once or twice a week. Sendai virus clearance was checked by Scorecard analysis and immunocytochemistry (data not shown). Quality controls of iPSC were performed as suggested by the International Stem Cell Banking Initiative [38]. To analyze iPSC spontaneous differentiation potential, iPSC were treated with collagenase (Thermo Fisher Scientific) and cultured in suspension as embryoid bodies (EB) for 10 days in Essential 6 medium (Thermo Fisher Scientific). EB were then harvested and either treated with RNAzol RT (Euromedex) for RNA extraction or plated on Geltrex and cultured in fibroblast medium for another 10 days to induce differentiation. Both undifferentiated iPSC and EB were fixed in 4% PFA (Euromedex) for 20 min and then incubated overnight at 4 °C with primary antibodies in blocking solution (1% BSA and 2% normal goat serum in 1X PBS) supplemented with 0.01% Triton-X100. Primary antibodies against TRA1-60, SSEA-4, SSEA-1, β-Catenin, Nestin, SMA, and NANOG were used [listed in suppl. Table 1 (Online Resource 8)]. Secondary antibodies were incubated in blocking solution for 1 h at room temperature. Nuclei were stained with Hoechst H33342 (Thermo Fisher Scientific). Slides were mounted with Fluoromount G (Southern Biotech). Images were captured on a Carl Zeiss AxioScope A1 with ZEN acquisition software. To standardize the characterization of iPSC, RNA extracted from iPSC and EB was analyzed using the TaqMan® hPSC Scorecard™ Panel (Thermo Fisher Scientific). This real-time PCR assay compares expressions of 94 q-PCR assays (composed of a combination of control, housekeeping, self-renewal, and lineage-specific genes) between samples and a reference set of nine human iPSC and ESC clones. Results are expressed as a score relative to the reference set. Genome integrity was assessed by Illumina Infinium®HumanCore-24 (> 300,000 markers) (Integragen, Evry, France) and analyzed using Illumina GenomeStudio and Karyostudio softwares (CELIS-iPS, ICM, France).

Motor neurons derived from iPSC

Motor neurons were differentiated from iPSC using previously described and validated protocols [17, 24] with some modifications. Briefly, iPSC clones were detached by Accutase treatment to form small clusters. Cells were transferred in Neuronal basic medium (DMEM/F12 plus Neurobasal medium with N2 and B27 supplement without vitamin A) supplemented with 40 µM SB431542 (Tocris Bioscience), 0.2 µM LDN-193189 (Stemgent), 3 µM CHIR99021 (Tocris Bioscience), and 5 µM Y-27632 (Merck Millipore) to induce EB formation. From day 3 on, 0.1 µM retinoic acid (Sigma) and 500 nM SAG (Merck Millipore) were added to the neuronal basic medium and medium was changed every 2 days. From day 9 on, BDNF (10 ng/ml, Miltenyi Biotec) and GDNF (10 ng/ml, Miltenyi Biotec) and DAPT (20 µM, Tocris Bioscience) were added. On day 10, floating clusters were dissociated into single cells using 0.05% trypsin (Gibco™). Motor neurons were seeded on laminin (20 µg/ml)-coated 24-well plates at the density of $0.2–2 \times 10^5$ cells per well. From day 17 on, the cells were switched to motor neuron maturation medium supplemented with BDNF, GDNF, CNTF and IGF (each 10 ng/ml, Miltenyi Biotec) to keep long-term cultures. Media were changed every 2 days by replacing half of the medium. For caspase activity measurement, motor neurons were treated either with 0.5 µM Staurosporine (Sigma) for 24 h or 50–100 µM glutamate (Sigma) for 48 h.

Immunocytochemistry

Cells plated on coverslips were fixed in 4% PFA for 20 min at room temperature and were washed with PBS. Permeabilization and blocking were performed for 30 min using PBS containing 0.1% Triton X-100 (Acros Organics) and 3% BSA (Sigma) for 1 h. Cells were incubated overnight at 4 °C in blocking buffer containing the different primary antibodies [listed in suppl. Table 1 (Online Resource 8)]. After washing with PBS, cells were incubated with secondary antibodies (Invitrogen) and DAPI (0.5 µg/ml, Molecular Probes) for 1 h at room temperature. Cells were washed, mounted with Fluoromount G (SouthernBiotech), and observed on a laser-scanning confocal microscope Nikon A1R. Confocal images were acquired with a Apochromat 40×/1.25 NA oil objective lens and were collected using 405, 488 and 561 nm laser lines for excitation and appropriate emission

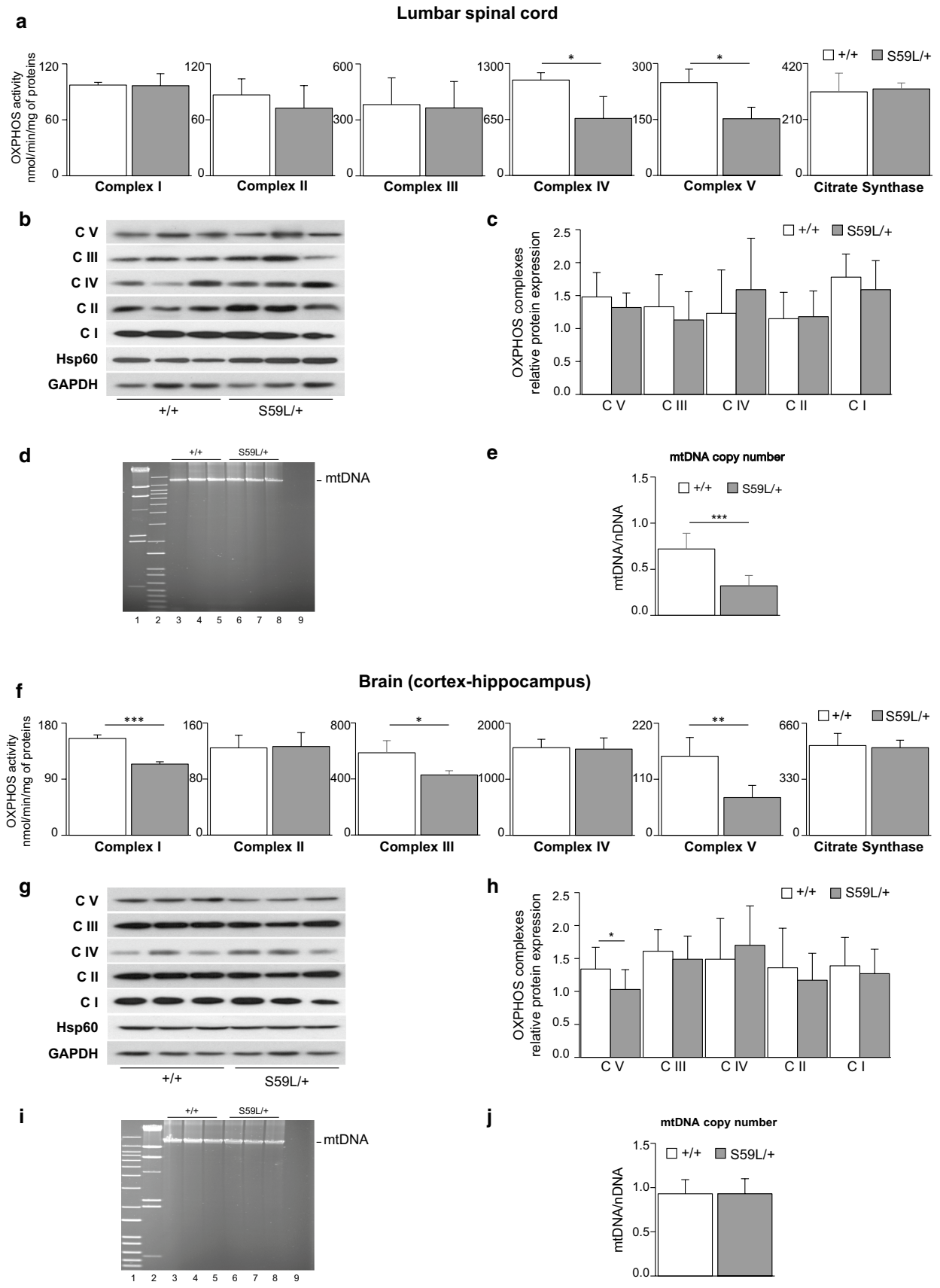
Lumbar spinal cord
a
OXPHOS activity nmol/min/mg of proteins
+/+
S59L/+
Complex I
Complex II
Complex III
Complex IV
Complex V
Citrate Synthase
b
C V
C III
C IV
C II
C I
Hsp60
GAPDH
c
OXPHOS complexes relative protein expression
d
mtDNA
e
mtDNA copy number
mtDNA/nDNA
Brain (cortex-hippocampus)
f
g
h
i
j

◂**Fig. 4** Mitochondrial analysis in lumbar spinal cord and brain from *CHCHD10*$^{S59L/+}$ mice at end stage. **a** Spectrophotometric analysis of respiratory chain in lumbar spinal cord from +/+ (white) and S59L/+ (gray) mice. Results represent the mean ± SD of 3 +/+ and 3 S59L/+ mice. **b** Representative western blot analysis from equal amounts (10 µg) of spinal cord homogenates of +/+ and S59L/+ mice using OXPHOS antibodies cocktail detecting complexes I–V, anti-Hsp60 and anti-GAPDH antibody for loading control. **c** Quantification of relative intensities of OXPHOS proteins shown in **b**. Data are shown as the mean ± SD of 4–7 independent experiments ($n = 3$ +/+ and 3 S59L/+ mice). **d** Long extension PCR of mtDNA from lumbar spinal cord of 3 +/+ (lanes 3–5) and 3 S59L/+ (lanes 6–8) mice. mtDNA indicates the 12.8 kb amplicon. Lanes 1, 2: molecular weight markers. Lane 9: PCR negative control. **e.** Mitochondrial DNA quantification in lumbar spinal cord of +/+ or S59L/+ mice. The mouse mitochondrial 12S rRNA (mtDNA) and the nuclear GAPDH (nDNA) genes were individually amplified by real-time PCR. Data were expressed as ratio between mtDNA and nDNA concentration. Results represent the mean of relative PCR ± SD of 3 independent experiments from 3 +/+ and 3 S59L/+ mice. **f** Spectrophotometric analysis of respiratory chain in brain (cortex and hippocampus) from +/+ and S59L/+ mice. Results represent the mean ± SD of 3 +/+ and 3 S59L/+ mice. **g** Representative western blot analysis from equal amounts (10 µg) of brain (cortex and hippocampus) homogenates of +/+ and S59L/+ mice using the same OXPHOS antibodies cocktail as in **b**. **h** Quantification of relative intensities of OXPHOS proteins shown in **g** (GAPDH was used as a loading control). Data are shown as the mean ± SD of 4–7 independent experiments ($n = 3$ +/+ and 3 S59L/+ mice). **i** Long extension PCR of mtDNA from brain (cortex and hippocampus) of 3 +/+ (lanes 3–5) and 3 S59L/+ (lanes 6–8) mice. mtDNA indicates the 12.8 kb amplicon. Lanes 1, 2: molecular weight markers. Lane 9: PCR negative control. **j** Mitochondrial DNA quantification in brain (cortex and hippocampus) of +/+ or S59L/+ mice. Data were expressed as ratio between mtDNA and nDNA concentration as in **e**. Results represent the mean of relative PCR ± SD of 3 independent experiments from 3 +/+ and 4 S59L/+ mice. The data from S59L/+ mice were compared to the controls. Statistical analysis was performed using Mann–Whitney's test in **c**, **e**, **h** and **j**, and Student's *t* test in **a** and **f**. *P* value = *< 0.05, **< 0.01, ***< 0.001

filters performed on a confocal microscope (Nikon A1R) with a 40× oil immersion lens.

Electron microscopy

Cells were seeded on 24 wells/plate, fixed with 1.6% glutaraldehyde in 0.1 M cacodylate buffer (pH 7.4) for 2 h, rinsed and postfixed in 1% osmium tetroxide and 1% potassium ferrocyanide in 0.1 M cacodylate buffer before to process for ultrastructure analysis as previously described [2]. Motor neurons were identified by their morphology and analyzed using a JEOL JEM1400 transmission electron microscope (JEOL, Tokyo, Japan). The length of mitochondria was traced and measured with ImageJ software.

Cell death measurement

NSC-34 and MEF cells were treated with 1 µM Staurosporine (Sigma-Aldrich), re-suspended and incubated in 200 µl of buffer containing 150 mM NaCl, 10 mM HEPES, 5 mM KCl, 1 mM $MgCl_2$, 1.8 mM $CaCl_2$ and annexin V-FITC (1/100) (Miltenyi Biotec) for 10 min at room temperature. DAPI (Molecular Probes) was then added, and samples were analyzed immediately by flow cytometry using an MACS-Quant Analyzer (Miltenyi Biotec).

Caspase activity measurement

Cells were treated either with Staurosporine or glutamate, and caspase activation was analyzed by DEVDase activity measurement as previously described [41]. Briefly, cells were lysed and after normalized to protein content, lysates were loaded into a black 96-well plate in the presence of 0.2 mmol/l of the caspase-3 substrate Ac-DEVD-AMC. Caspase activity was measured using a fluoroscan at 460 nm, and specific activity was expressed as the change in absorbance per minute per milligram protein.

Statistical analysis

Statistical analysis was done with one-way analysis of variance (ANOVA) followed by Bonferroni's post hoc comparison test, two-way ANOVA followed by Tukey's multiple comparison test, Log-rank (Mantel-Cox) test, Student's *t* test or Mann–Whitney's test. The quantitative data were analyzed in Microsoft Excel and GraphPad Prism (GraphPad Software). Data are means ± SD or ± SEM. "*n*" represents number of mice or cells per experiment. The data from S59L/+ mice were compared to the controls. *P* value = *< 0.05, **< 0.01, ***< 0.001.

Results

CHCHD10$^{S59L/+}$ mice present a lethal phenotype before 14 months of age

Using homologous recombination, we generated KI mice carrying the p.Ser59leu mutation. The strategy for genotyping is shown in Fig. 1a, b. Sequencing of cDNA was performed to confirm the presence of the mutation at the RNA level in the mouse genome (Fig. 1c). *CHCHD10*$^{S59L/+}$ mice were born at normal Mendelian ratios, weighted the same as WT littermates and appeared normal. From 10 weeks of age, *CHCHD10*$^{S59L/+}$ mice failed to gain weight normally and were significantly leaner than controls despite normal to increased calorie intake (data

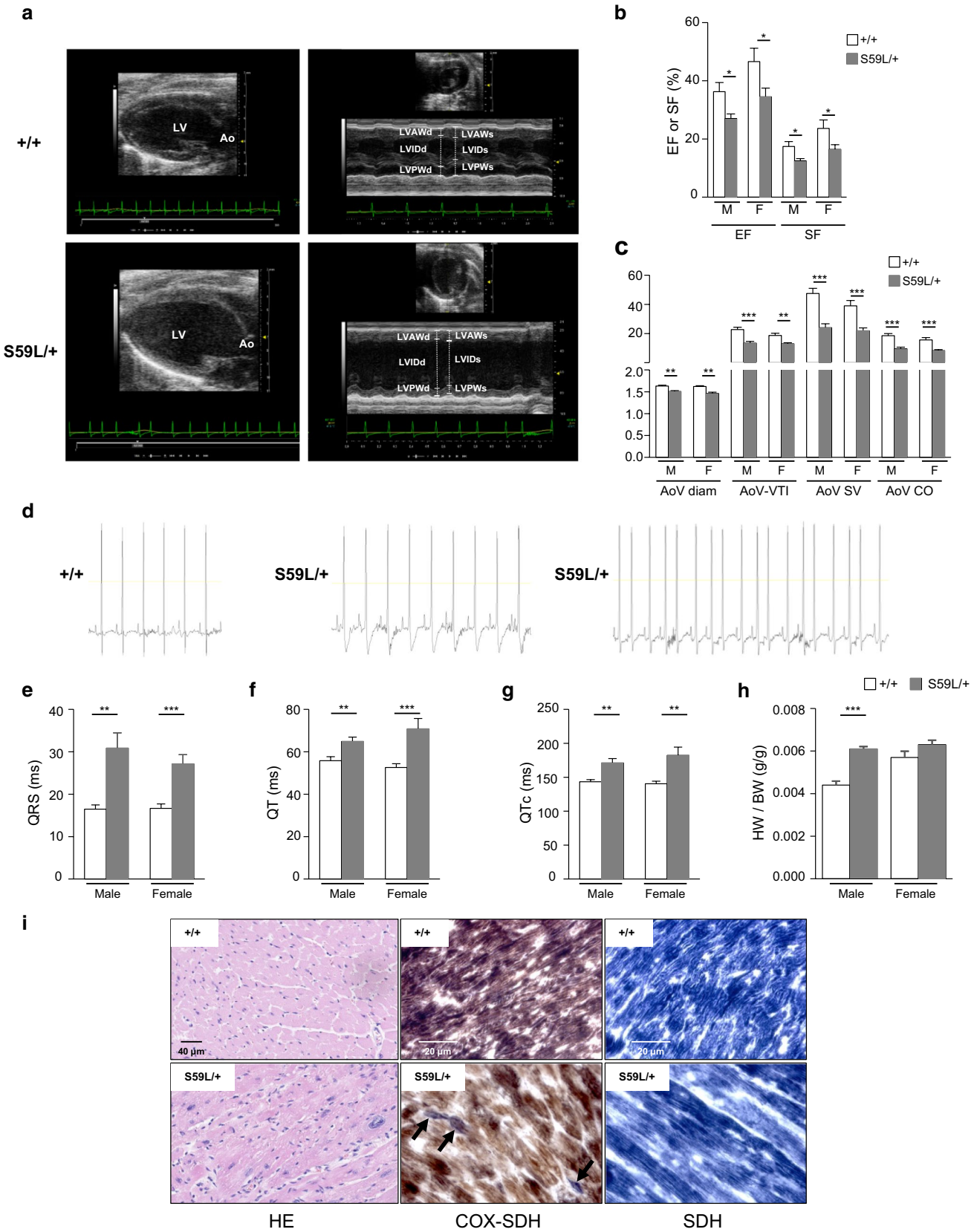
a
+/+
S59L/+
LV
Ao
LVAWd
LVAWs
LVIDd
LVIDs
LVPWd
LVPWs
b
EF or SF (%)
+/+
S59L/+
M
F
EF
SF
c
AoV diam
AoV-VTI
AoV SV
AoV CO
d
e
QRS (ms)
f
QT (ms)
g
QTc (ms)
h
HW / BW (g/g)
Male
Female
i
40 µm
20 µm
HE
COX-SDH
SDH

◂**Fig. 5** Heart disease in *CHCHD10*$^{S59L/+}$ mice. **a** Echocardiography performed on +/+ (upper panels) and S59L/+ mice (lower panels). Parasternal long axis view of the left ventricle showing the difference of structure between +/+ and S59L/+ mice (left panels). Parasternal short axis view and M-mode image of the left ventricle showing the difference of systolic function between +/+ and S59L/+ mice (right panels). *LV* left ventricle, *Ao* aorta, *LVAW* left ventricle anterior wall, *LVID* left ventricle internal dimensions, *LVPW* left ventricle posterior wall, *d*, *s* diastole and systole, respectively. Cardiac systolic function: ejection fraction (EF) and shortening fraction (SF) (**b**) and aortic artery function (**c**). Data are mean ± SEM from 10 +/+ males, 10 S59L/+ males, 9 +/+ females and 10 S59L/+ females at 24 weeks. *AoV diam* aortic artery diameter, *VTI* velocity time intergral, *SV* stroke volume, *CO* cardiac output. **d** ECG signals of +/+ (left panel) and mutant (middle and right panels) mice showing arrhythmia (middle panel) and ST segment abnormality (right panel). **e**–**g** ECG intervals analysis. QRS (**e**) represents the duration of ventricle depolarization, QT (**f**) and QTc (**g**) represent the ventricle repolarization. Data are mean ± SEM from 10 +/+ males, 10 S59L/+ males, 9 +/+ females and 10 S59L/+ females at 24 weeks. **h** Heart weight (HW) measurement adjusted to body weight (BW). Data are mean ± SEM from 9 +/+ and 10 S59L/+ mice (for each gender) at 31 weeks. **i** Histopathology of heart from +/+ (upper panels) and S59L/+ (lower panels) mice with HE (left panels), COX-SDH (middle panels) and SDH (right panels) stainings. The arrows indicate COX-negative fibers in mutant animals. The data from S59L/+ mice were compared to the controls. Statistical analysis was performed using Student's *t* test in **b**, **c**, **e**–**h**. *P* value = *< 0.05, **< 0.01, ***< 0.001

not shown), reflecting hypercatabolism (Fig. 1d). Between 6 months and 1 year, they began losing weight rapidly. Mice also developed tremors and were euthanized for ethical reasons when loosing 15% of their maximal body weight (Fig. 1e) [S1 Movie (Online Resource 1): KI mouse at end stage (1 year of age); S2 Movie (Online Resource 2): WT littermate]. Kaplan–Meier survival analysis revealed that *CHCHD10*$^{S59L/+}$ mice had a significantly reduced survival when compared with their WT littermates with an average survival of 10.13 and 11.42 months and a median survival of 10.33 and 11.4 months in males and females, respectively (Fig. 1f). Western blot analysis showed higher expression level of CHCHD10 in peripheral and cardiac muscles than in brain and spinal cord both in WT and KI mice (Fig. 1g). We compared CHCHD10 expression levels in tissues from *CHCHD10*$^{S59L/+}$ and WT animals at 3 months of age. RT-qPCR analysis showed that mRNA levels were similar in skeletal muscle, heart, spinal cord and brain in mutant and WT mice (Fig. 1h). Quantification of western blot analysis (Fig. 1i, j) also showed no difference in protein levels.

Mitochondrial myopathy with mtDNA instability in *CHCHD10*$^{S59L/+}$ mice

In our original family, patients heterozygous for the p.Ser59Leu mutation presented a mitochondrial myopathy with mtDNA deletions [2]. Similarly, we observed that, at the end stage, muscle of *CHCHD10*$^{S59L/+}$ mice revealed irregular-sized muscle fibers but no ragged-red fibers (RRF) (Fig. 2a). We found no COX-negative fibers but low levels of COX (complex IV) and SDH (complex II) expression compared with WT littermates (Fig. 2b, c). These results were confirmed by western blots (Fig. 2d). Electron microscopy of skeletal muscles revealed altered morphology of mitochondria and cristae organization in KI animals (Fig. 2e–g). Spectrophotometric analyses showed a generalized respiratory chain (RC) deficiency (Fig. 2h). We found mtDNA deletions by long-range PCR (Fig. 2i) and the determination of relative mtDNA copy number by real-time quantitative PCR showed a significant depletion compared with controls (Fig. 2j). Mitochondrial disease in mutant mice was further supported by increased blood lactate levels in KI mice compared to WT littermate (Fig. 2k).

Altogether, we established that KI mouse phenotype mimics a mitochondrial myopathy with mtDNA instability as observed in patients carrying the *CHCHD10* p.Ser59Leu mutation.

CHCHD10$^{S59L/+}$ mice display neuromuscular junction and motor neuron degeneration with TDP-43 proteinopathy at end stage

In addition to their involvement in mitochondrial myopathy, *CHCHD10* mutations have also been associated with MND. Because degeneration of neuromuscular junction (NMJ) is considered a key and early feature in ALS patients [32, 43], we focused our attention on the synaptic morphology of KI animals. NMJ is composed of three elements: pre-synaptic (motor nerve terminal), intrasynaptic (synaptic basal lamina) and post-synaptic part (motor end plate of muscle cell). At the end stage, NMJs from *CHCHD10*$^{S59L/+}$ mice and control littermates were immunohistochemically labeled, imaged and analyzed using "NMJ-morph" [21] (Fig. 3a). We identified significant differences in the morphology of the post-synaptic part of NMJs between mutant and WT animals. Fluorescently labeled α-bungarotoxin was used to delineate the post-synaptic membrane of the NMJ as it binds tightly to the acetyl choline receptors (AChRs) found at this membrane. The compactness of AChRs (referring to a quantity of post-synaptic receptors within a given area) [21] was significantly higher at the motor end plate from *CHCHD10*$^{S59L/+}$ mice compared with control littermates (Fig. 3b) and the motor end plate of KI animals also presented a higher degree of fragmentation (Fig. 3c). As shown in Fig. 3d, double immunofluorescent staining patterns of α-bungarotoxin and CHCHD10 suggest that CHCHD10 is concentrated at the post-synaptic vicinity of the NMJ but is not co-localized with the AChRs. CHCHD10 labeling was consistent with localization within mitochondria, which accumulate in the

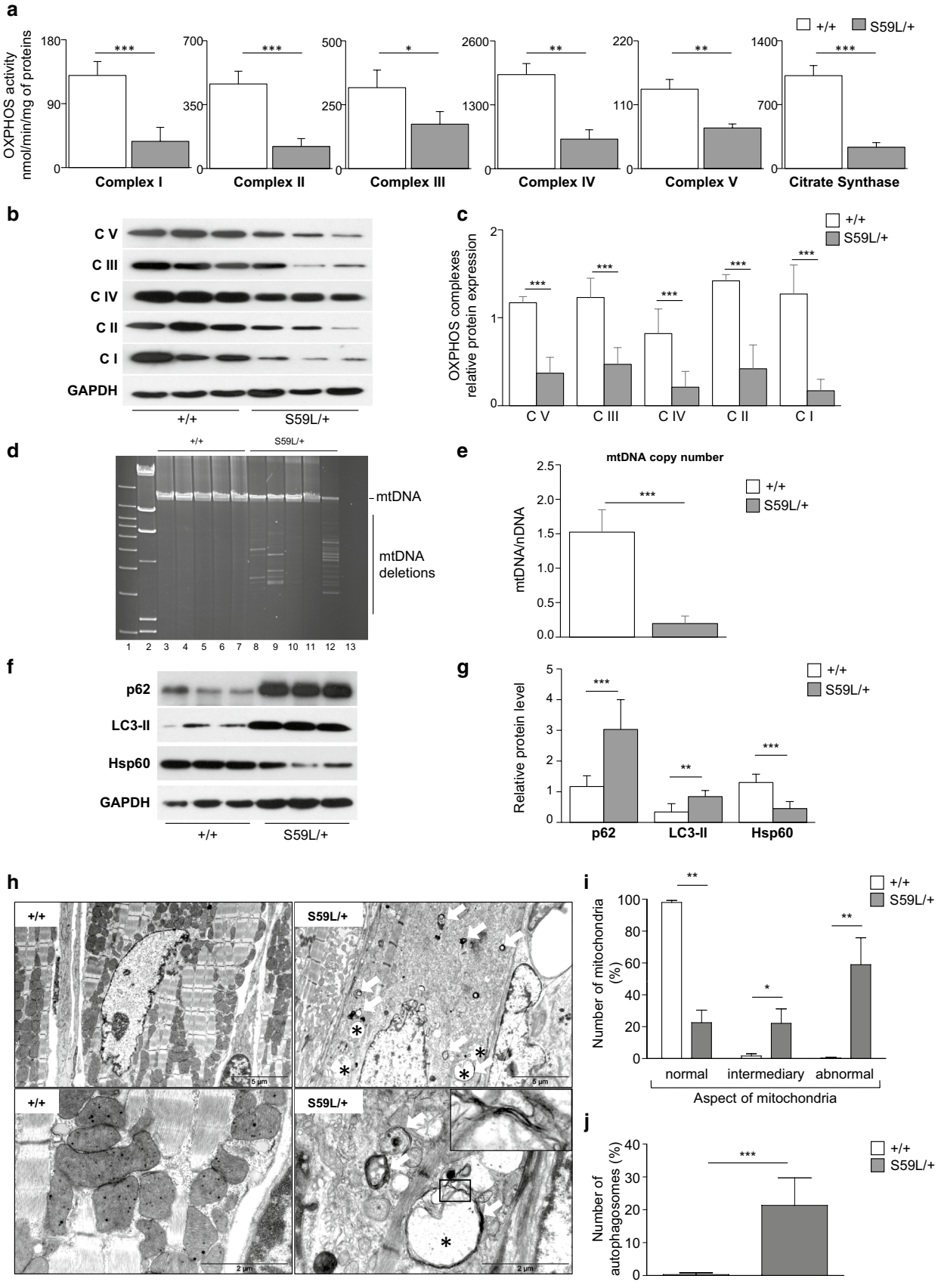
a
OXPHOS activity nmol/min/mg of proteins
+/+
S59L/+
Complex I
Complex II
Complex III
Complex IV
Complex V
Citrate Synthase
b
C V
C III
C IV
C II
C I
GAPDH
c
OXPHOS complexes relative protein expression
d
mtDNA
mtDNA deletions
e
mtDNA copy number
mtDNA/nDNA
f
p62
LC3-II
Hsp60
g
Relative protein level
h
5 µm
2 µm
i
Number of mitochondria (%)
normal
intermediary
abnormal
Aspect of mitochondria
j
Number of autophagosomes (%)

◂**Fig. 6** OXPHOS and autophagy/mitophagy in the heart of *CHCHD10*$^{S59L/+}$ mice at end stage. **a** Spectrophotometric analysis of respiratory chain in heart from +/+ and S59L/+ mice. Results represent the mean ± SD of 3 +/+ and 3 S59L/+ mice. **b** Representative western blot analysis from equal amounts (2.5 µg) of heart homogenates of +/+ and S59L/+ mice using OXPHOS antibodies cocktail detecting complexes I–V and anti-GAPDH antibody for loading control. **c** Quantification of relative intensities of OXPHOS proteins shown in **b** Data are shown as the mean ± SD of 3 independent experiments (n = 3 +/+ and 3 S59L/+ mice). **d** Long extension PCR of mtDNA from heart of 5 +/+ (lanes 3–7) and 5 S59L/+ (lanes 8–12) mice. mtDNA indicates the 12.8 kb amplicon. Lanes 1, 2: molecular weight markers. Lane 13: negative PCR control. **e** Mitochondrial DNA quantification in muscle of +/+ or S59L/+ mice. The mouse mitochondrial 12S rRNA (mtDNA) and the nuclear GAPDH (nDNA) genes were individually amplified by real-time PCR. Data were expressed as ratio between mtDNA and nDNA concentration. Results represent the mean of relative PCR ± SD of 3 independent experiments from 5 +/+ and 5 S59L/+ mice. **f** Representative western blot of LC3-II, p62, Hsp60 and GAPDH expression levels from equal amounts (2.5 µg) of heart homogenates of +/+ and S59L/+ mice. **g** Quantification of relative intensities of LC3-II, p62 and Hsp60 proteins shown in **f** (GAPDH was used as a loading control). Data are shown as the mean ± SD of 3–4 independent experiments (n = 3 +/+ and 3 S59L/+ mice). **h** Ultrastructure of heart from +/+ (left panels) and S59L/+ (right panels) animals showing myofibrillar disorganization with vacuolated mitochondria (*) and autophagosomes (arrows) in S59L/+ mice. Scale bar: 5 µm (upper panels) and 2 µm (lower panels). Quantification of mitochondrial morphology (**i**) and autophagosome number (**j**) observed in **h**. Intermediary refers to mitochondria that cannot be clearly classified as abnormal despite the presence of slight cristae anomalies. Shown are mean ± SEM (n = 3 +/+ and 3 S59L/+ mice with at least 100 mitochondria per animal randomly chosen and analyzed). Statistical analysis was performed using Student's t test in **a**, **i** and **j** and Mann–Whitney's test in **c**, **e** and **g**. P value = *< 0.05, **< 0.01, *** < 0.001

post-synaptic region of the NMJ and within mitochondria from muscle fiber. Interestingly, in *CHCHD10*$^{S59L/+}$ mice, the fragmentation of the motor end plate was associated with abnormal expression of CHCHD10 that was also observed when NMJs were morphologically normal [Fig. 3d; suppl. Figure 1 (Online Resource 3)]. In ALS patients and animal models, NMJ degeneration precedes motor neuron loss. The number of large Nissl-stained cells representative of motor neurons in the lumbar spinal cord (L3–L6) of *CHCHD10*$^{S59L/+}$ mice was significantly lower than that in WT littermates at the end stage (15.17% neuron loss) (Fig. 3e, f). In ALS and in FTD patients, TDP-43 proteins form insoluble aggregates in neuronal cytoplasm, also known as TDP-43 proteinopathy. We found TDP-43 cytoplasmic aggregates in spinal neurons of *CHCHD10*$^{S59L/+}$ mice at the end stage of the disease (Fig. 3g, h). All these findings indicate that at the stage when we had to kill the animals, KI mice presented signs of motor neuron degeneration.

We next analyzed mitochondrial functions in spinal cord and brain. At the end stage, spectrophotometric analysis of lumbar spinal cord from *CHCHD10*$^{S59L/+}$ mice showed a defect of complexes IV and V activities (Fig. 4a) that was not associated with decreased levels of RC proteins (Fig. 4b, c). We did not detect mtDNA deletion by long-range PCR (Fig. 4d) but real-time quantitative PCR analysis revealed a significant reduction of mtDNA copy number (Fig. 4e). Electron microscopy analysis revealed no ultrastructural abnormalities of motor neurons except at the mitochondrial level with cristae disorganization [suppl. Figure 2 (Online Resource 4)]. A multiple RC deficiency was also observed in the brain (cortex and hippocampus) of the mutant mice (Fig. 4f) without decrease of RC protein levels (Fig. 4g, h). Analysis of mtDNA identified neither deletion (Fig. 4i) nor depletion (Fig. 4j). These results suggest that mitochondrial dysfunction and oxidative phosphorylation (OXPHOS) deficiency are much higher in muscle than in lumbar spinal cord and in brain from mutant animals at end stages.

We studied the clinical and electrophysiological consequences of the neuromuscular alterations found in KI mice between 20 and 26 weeks. When analyzed for specific motor abilities, both male and female KI performed as well as WT animals during rotarod, grip and string tests [suppl. Figure 3a–c (Online Resource 5)]. KI mice also had normal proprioceptive abilities as reflected by the number of hind paws slips comparable to that of WT [suppl. Figure 3d (Online Resource 5)]. Electromyographical recording (EMG) showed that mutant mice had normal SNCV and CMAP evoked by sciatic nerve stimulation [suppl. Figure 3e–g (Online Resource 5)]. Nevertheless, none of the above analyses was done after 26 weeks of age to analyze a population of sufficient size (10 *CHCHD10*$^{S59L/+}$ and 10 *CHCHD10*$^{+/+}$ mice of each sex) and they do not reflect what is happening at end stage.

CHCHD10$^{S59L/+}$ mice develop a fatal cardiomyopathy associated with enhanced mitophagy

The neurological signs observed in KI mice are likely not responsible for the acute decompensation they present at the end stage of the disease. The heart, being highly energy dependent and particularly vulnerable to impaired OXPHOS, we performed echography in KI and WT mice at 23 weeks of age. All mutant animals presented a cardiomyopathy with a severe systolic dysfunction (Fig. 5a). A significant decrease in ejection fraction, shortening fraction and aortic flow rate was found both in male and female KI mice (Fig. 5b, c). Electrocardiography (ECG) showed junctional extra systoles with arrhythmia in several KI mice compared with WT littermates and all mutant animals presented changes in ST segment morphology (Fig. 5d) with significant prolonged QRS, QT and QTc intervals (Fig. 5e–g). Heart weight adjusted to body weight was increased in KI mice (Fig. 5h). Heart histology revealed a significant vacuolization of cardiomyocytes in KI animals with owl eye-shaped nuclei and signs of interstitial inflammation (Fig. 5i). Gomori modified

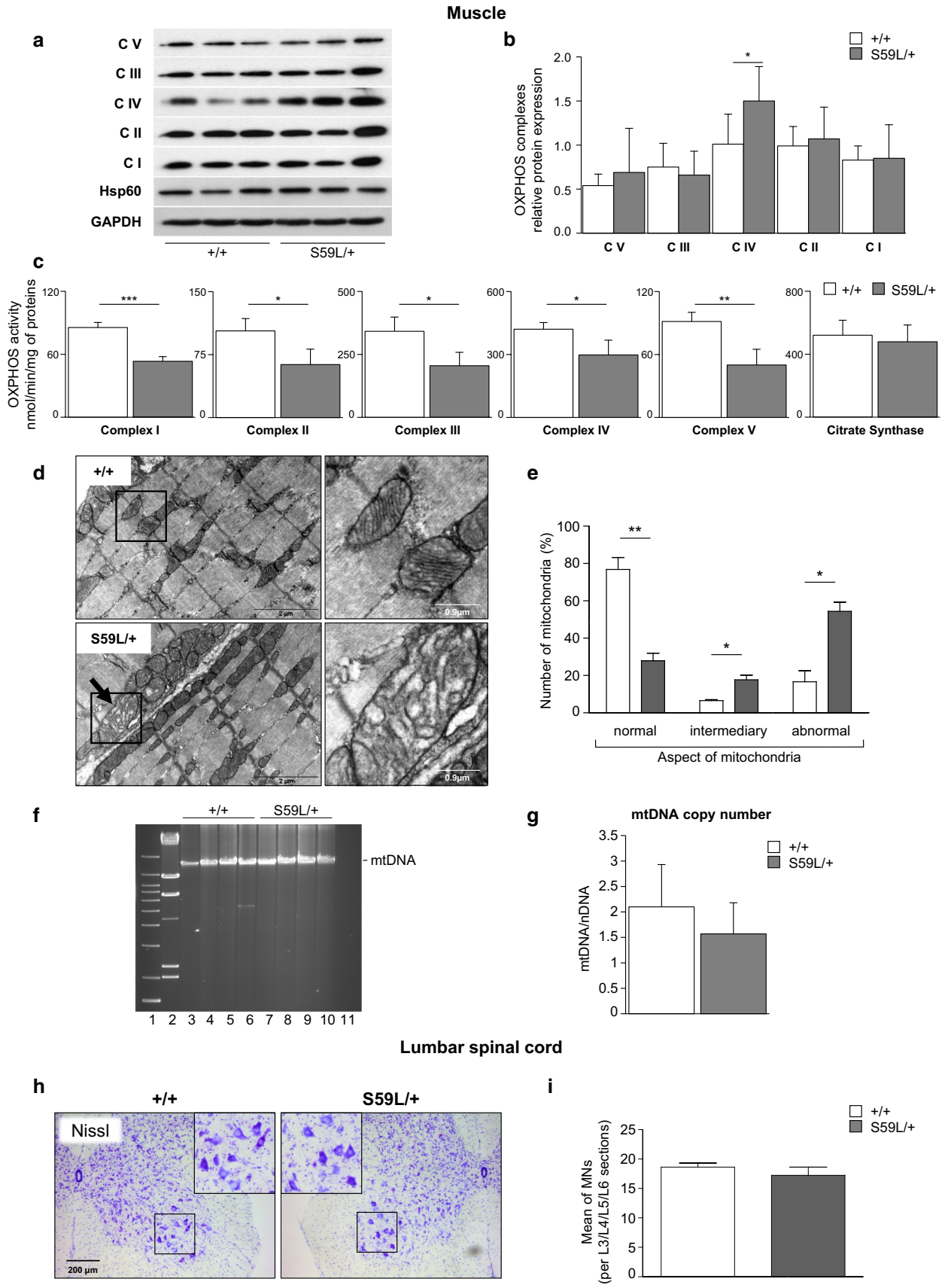
Muscle
a
C V
C III
C IV
C II
C I
Hsp60
GAPDH
+/+
S59L/+
b
+/+
S59L/+
OXPHOS complexes relative protein expression
C V
C III
C IV
C II
C I
c
OXPHOS activity nmol/min/mg of proteins
Complex I
Complex II
Complex III
Complex IV
Complex V
Citrate Synthase
d
+/+
S59L/+
2 µm
0.9µm
e
Number of mitochondria (%)
normal
intermediary
abnormal
Aspect of mitochondria
f
+/+
S59L/+
mtDNA
1 2 3 4 5 6 7 8 9 10 11
g
mtDNA copy number
mtDNA/nDNA
+/+
S59L/+
Lumbar spinal cord
h
+/+
S59L/+
Nissl
200 µm
i
Mean of MNs (per L3/L4/L5/L6 sections)
+/+
S59L/+

◂**Fig. 7** Muscle and motor neuron analysis of *CHCHD10*$^{S59L/+}$ mice at 3 months of age. **a** Representative western-blot analysis from equal amounts (2.5 µg) of muscle homogenates of +/+ and S59L/+ mice using OXPHOS antibodies cocktail detecting complexes I–V, anti-Hsp60 and anti-GAPDH antibody for loading control. **b** Quantification of relative intensities of OXPHOS proteins from +/+ (white) and S59L/+ (gray) mice (GAPDH was used as a loading control). Data are shown as the mean ± SD of 3 independent experiments ($n = 3$ +/+ and 3 S59L/+ mice). **c** Spectrophotometric analysis of respiratory chain in muscle from +/+ and S59L/+ mice. Results represent the mean ± SD of 3 +/+ and 3 S59L/+ animals. **d** Ultrastructure of skeletal muscle from +/+ and S59L/+ mice showing abnormal mitochondria (arrows) in mutant animals. Vacuolated mitochondria with abnormal cristae are visible in S59L/+ muscle. The right panel of each image is a magnification of the area indicated by the square in the left panel. Scale bars: 2 µm in left panels and 0.5 µm in right panels. **e** Quantification of mitochondrial morphology observed in **d**. Intermediary refers to mitochondria that cannot be clearly classified as abnormal despite the presence of slight cristae anomalies. Shown are mean ± SEM ($n = 2$ +/+ and 3 S59L/+ mice with at least 70 mitochondria per animal randomly chosen and analyzed). **f** Long extension PCR of mtDNA from muscle of 4 +/+ (lanes 3–6) and 4 S59L/+ (lanes 7–10) mice. mtDNA indicates the 12.8 kb amplicon. Lanes 1, 2: molecular weight markers. Lane 11: negative PCR control. **g** Mitochondrial DNA quantification in muscle of +/+ or S59L/+ mice. The mouse mitochondrial 12S rRNA (mtDNA) and the nuclear GAPDH (nDNA) genes were individually amplified by real-time PCR. Data were expressed as ratio between mtDNA and nDNA concentration. Results represent the mean of relative PCR ± SD of 3 independent experiments from 5 +/+ and 6 S59L/+ mice. **h** Nissl staining of lumbar spinal cords from +/+ and S59L/+ mice showing large motor neurons (insets). Scale bar: 200 µm. **i** Quantification of motor neurons in the ventral horns of lumbar spinal cord (between L3 and L6 sections). Shown are mean ± SEM ($n = 4$ +/+ and 4 S59L/+ mice with 20 sections per animal randomly chosen and analyzed). The data from S59L/+ mice were compared to the controls. Statistical analysis was performed using Mann–Whitney's test in **b**, **g** and **i**, and Student's *t* test in **c** and **e**. *P* value = *< 0.05, **< 0.01, ***< 0.001

trichrome showed no RRF (not shown) but COX-negative fibers were observed in all mutant animals that were analyzed (Fig. 5i). At the end stage, spectrophotometric analysis of RC enzyme activities confirmed OXPHOS impairment by showing a generalized defect in KI animals (Fig. 6a) with a significant decrease in the expression level of all RC complexes by western blot analysis (Fig. 6b, c). Long-range PCR revealed small amounts of mtDNA deletions in the heart of KI animals, which also displayed a severe loss of mtDNA copies (Fig. 6d, e).

The low level of citrate synthase activity and the dramatic loss of mtDNA molecules suggested a mitochondrial mass lowering. The vacuolization observed in the cardiomyocytes may also be evocative of autophagic vacuole formation [19]. We, therefore, evaluated the involvement of autophagy in the cardiomyopathy of the *CHCHD10*$^{S59L/+}$ mice. Western blot analysis revealed both significantly increased LC3-II, p62 levels and decreased Hsp60 levels in KI animals as compared with WT littermates (Fig. 6f, g). Autophagosomes were rarely seen in the heart of the WT mice under electron microscopy whereas numerous autophagosomes engulfing mitochondria were observed in the heart of KI littermates at end stages (Fig. 6h). Loss and disorganization of myofibrils with vacuolar mitochondria were also observed in cardiac tissue from *CHCHD10*$^{S59L/+}$ mice (Fig. 6h–j). We have, therefore, established that the p.Ser59Leu mutation leads to massive mitochondrial dysfunction in heart muscle that is associated with enhanced mitophagy and results in severe heart disease at the end stage.

Mitochondrial dysfunction in muscle from *CHCHD10*$^{S59L/+}$ mice precedes motor neuron degeneration

To analyze the sequence of pathological events associated with the expression of the p.Ser59Leu allele, we analyzed the muscle of *CHCHD10*$^{S59L/+}$ mice at 3 months of age, which corresponds to the moment when they began to show a lower body mass with their WT littermates. At this stage, muscle histological analysis was normal (not shown) as well as OXPHOS protein levels (Fig. 7a, b). However, we identified a generalized defect of the mitochondrial RC in the muscle of *CHCHD10*$^{S59L/+}$ mice by spectrophotometry (Fig. 7c) and electron microscopy identified abnormal mitochondria with cristae disorganization in the muscle of young *CHCHD10*$^{S59L/+}$ animals as compared with WT (Fig. 7d, e). We found no mtDNA deletion (Fig. 7f) and no significant decrease of mtDNA copy number in KI mice (Fig. 7g). We next focused on spinal cord and found that the number of neurons in the lumbar region (L3–L6) was similar in *CHCHD10*$^{S59L/+}$ mice and WT littermates (Fig. 7h, i). Importantly, these results suggest that muscle dysfunction with OXPHOS deficiency precedes motor neuron degeneration and that the lower motor neuron number measured in KI mice at end stage (Fig. 3e, f) was linked to a degeneration of motor neuron rather than fewer numbers from birth.

CHCHD10^{S59L} mutation increases the sensitivity of motor neurons to apoptosis

We previously reported that the p.Ser59Leu mutation decreases the sensitivity of HeLa and of human fibroblasts to stress-induced apoptosis [15]. In line with those results, we observed that mouse embryonic fibroblasts (MEFs) isolated from KI mice were less sensitive to Staurosporine (STS)-induced death than control MEFs [suppl. Figure 4a (Online Resource 6)]. It is well established that post-mitotic cells have a very different response to stress-induced death compared to proliferating cells (such as fibroblasts). We, therefore, investigated caspase activation in several organs of KI mice at the end point. We did not observe any significant caspase activation in the brain, the spinal cord or the skeletal muscle of the mice, that is in line with the absence of major

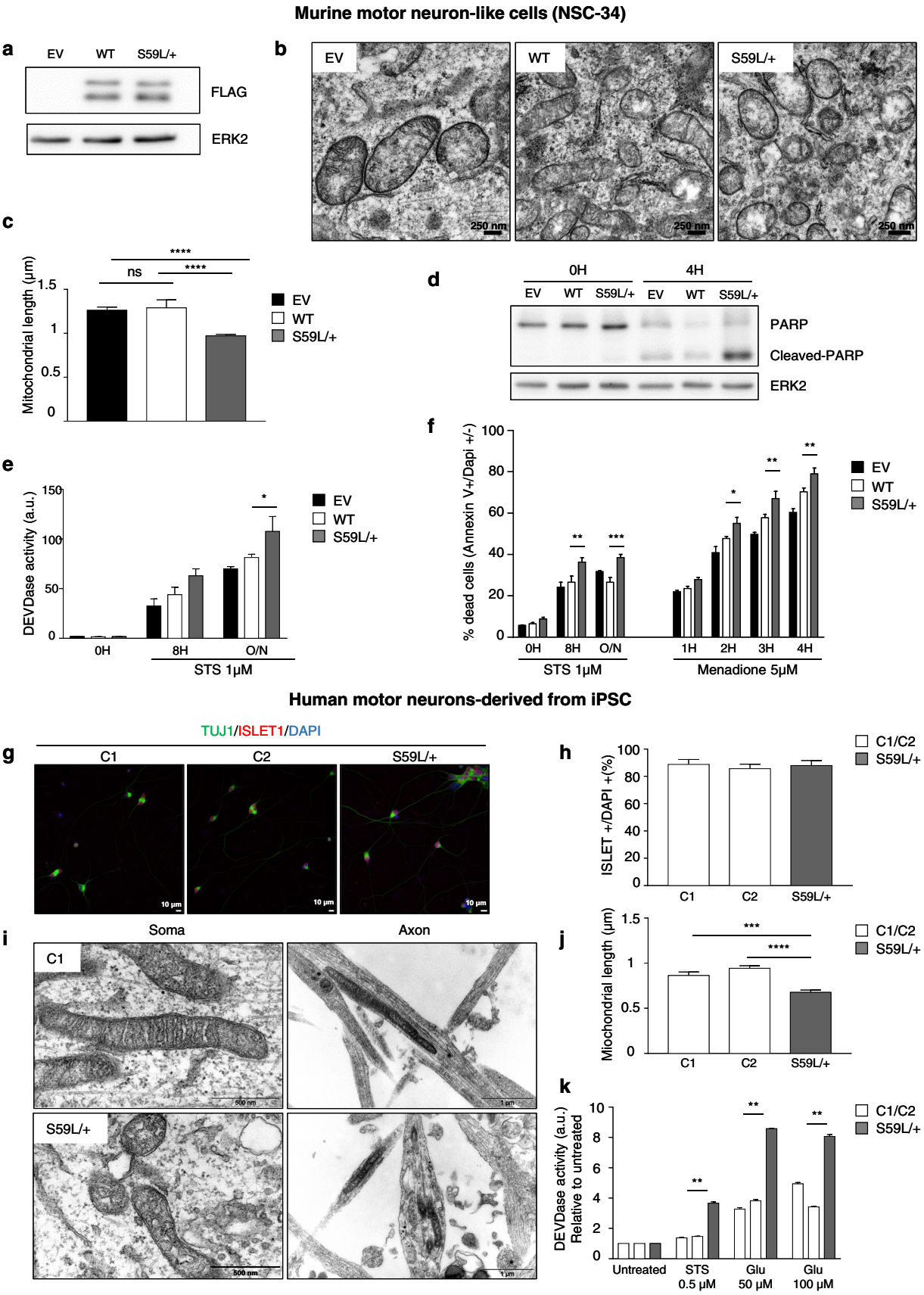
Murine motor neuron-like cells (NSC-34)
a
EV
WT
S59L/+
FLAG
ERK2
b
EV
WT
S59L/+
250 nm
c
Mitochondrial length (µm)
ns
****
EV
WT
S59L/+
d
0H
4H
EV WT S59L/+ EV WT S59L/+
PARP
Cleaved-PARP
ERK2
e
DEVDase activity (a.u.)
0H
8H
O/N
STS 1µM
f
% dead cells (Annexin V+/Dapi +/-)
0H 8H O/N 1H 2H 3H 4H
STS 1µM
Menadione 5µM
Human motor neurons-derived from iPSC
g
TUJ1/ISLET1/DAPI
C1
C2
S59L/+
10 µm
h
ISLET +/DAPI +(%)
C1/C2
S59L/+
i
Soma
Axon
C1
S59L/+
500 nm
1 µm
j
Miochondrial length (µm)
k
DEVDase activity (a.u.)
Relative to untreated
Untreated
STS 0.5 µM
Glu 50 µM
Glu 100 µM

◂**Fig. 8** The pSer59Leu mutation sensitizes motor neurons to cell death. **a** Western blot on NSC-34 cell extracts transfected with empty vector (EV) or vectors encoding human wild-type CHCHD10-FLAG (WT) or mutant CHCHD10-FLAG (S59L). Antibodies against FLAG or ERK2 (loading control) were used. **b** Ultrastructural analysis of NSC-34 cells transfected with EV, WT or S59L. Scale bar = 250 nm. **c** Measurement of mitochondrial length from transfected NSC-34 cells shown in **b** (at least 100 mitochondria per condition randomly chosen and analyzed). NSC-34 cells were treated with 1 µM Staurosporine (STS) for 8 h and 16 h (O/N). Caspase activation was determined either by western blot assessing the cleavage of PARP after 4 h of treatment (**d**) or by DEVDase activity measurement after 8 or 16 h (O/N) of treatment (**e**). Representative data of three independent experiments are shown. **f** NSC-34 cell death was determined by flow cytometry using Annexin V/DAPI staining after either 1 µM STS or 5 µM Menadione treatment. Three independent experiments were performed per condition. **g** Immunostaining of ISLET1, TUJ1 and DAPI in human motor neurons derived from iPSC after 35 days of differentiation (2 control clones (C1 and C2) and one S59L/+ clone). Scale bar = 10 µm. **h** Quantification of ISLET1-positive cells ($n = 77$, 103 and 121 cells for C1, C2 and S59L/+ clones, respectively) expressed relative to the total number of DAPI-labeled cells. Data are represented as mean ± SEM. **i** Ultrastructural analysis of control- and S59L/+-derived motor neurons at day 35. Representative images of both soma and axons. $n = 3$ independent experiments. Scale bars = 500 nm and 1 µm. **j** Measurement of mitochondria length from motor neurons derived from S59L/+ and control iPSC (C1 and C2) lines at day 35. **k** DEVDase activity was measured on motor neurons treated either with 0.5 µM STS for 24 h or glutamate (Glu) (50 µM and 100 µM) for 48 h. Data values represent mean ± SEM. Differences between groups were analyzed by two-way ANOVA (Tukey's multiple comparisons test). *P* value = *< 0.05, **< 0.01, ***< 0.001, ****< 0.0001

deficiency observed in the mice upon development and post birth. On the opposite, we found that KI mice presented an increased caspase activity and a higher active caspase level in the heart compared to WT littermates at the end stage [suppl. Figure 4b, c (Online Resource 6)]. This is very likely occurring as a consequence of fatal cardiomyopathy that is observed in the heart of the KI mice. As we observed early signs of motor neuron degeneration in KI mice at end point, we investigated if motor neurons expressing *CHCHD10*$^{+/+}$ or *CHCHD10*$^{S59L/+}$ alleles presented different sensitivity to apoptosis. Unfortunately, to address this crucial point we could not age KI mice further due to fatal cardiomyopathy. We, therefore, first used the mouse motor neuron-like hybrid cell line (NSC-34) in which we overexpressed either the WT or the p.Ser59Leu mutant of *CHCHD10* along with a FLAG-tag (Fig. 8a). As observed in our KI model, NSC-34 cells expressing the p.Ser59Leu mutation presented altered morphology of mitochondria and cristae organization (Fig. 8b), and a significant decrease in mitochondria length (Fig. 8c). As opposed to what was observed in fibroblasts, NSC-34 cells expressing the p.Ser59Leu mutant were significantly more sensitive to Staurosporine (STS)- and to ROS-induced death (using Menadione) compared to controls. This could be observed through an increased cleavage of the canonical caspase substrate PARP (Fig. 8d) that is associated with an increased caspase activity (DEVDase, Fig. 8e) and an increased proportion of annexin V/Dapi-positive cells (Fig. 8f). Finally, to investigate if human motor neurons carrying the p.Ser59Leu mutation were more sensitive to cell death, we generated iPSC from fibroblasts of a control and a patient carrying the p.Ser59Leu variant [2]. Those iPSC were then differentiated in human motor neurons allowing us to study the impact of the mutation on the sensitivity of human motor neurons to apoptosis [suppl. Figure 4d–g (Online Resource 6)]. We did not observe significant differences between WT and p.Ser59Leu cells neither in the ability of the iPSC to differentiate into motor neurons (Fig. 8g, h) nor in the viability of iPSC-derived motor neurons [suppl. Figure 4h (Online Resource 6)]. *CHCHD10*$^{S59L/+}$ motor neurons displayed mitochondria with altered morphology (Fig. 8i), and a significant decreased length (Fig. 8j) as we observed in NSC-34 cells, in KI mice and previously in patient fibroblasts carrying the heterozygous p.Ser59Leu mutation. Importantly, S59L/+ motor neurons were much more sensitive to STS- or glutamate-induced caspase activation than control cells (Fig. 8k). Glutamate-induced excitotoxicity is well known as a major contributor to dysfunction and death of motor neurons in the pathogenesis of ALS [4, 40]. Collectively, our data indicate that the p.Ser59Leu mutation sensitized motor neurons to stress-induced death.

Discussion

Although primary mitochondrial diseases rarely manifest with MND, mitochondrial dysfunction is an important factor associated with motor neuron degeneration [7, 37]. However, our understanding of the nature of the initial modulation leading to mitochondrial dysfunction and the subsequent sequence of events leading to motor neuron death remains largely unknown. The *CHCHD10* gene was recently involved in mitochondrial disorders and neurodegenerative diseases. However, there is only a few numbers of functional studies regarding the effects of *CHCHD10* mutations in patient fibroblasts or in neuron cell lines overexpressing *CHCHD10* variants [14, 15, 44]. We thus decided to generate new models including KI mice and human iPSC expressing the p.Ser59Leu mutation responsible for both mitochondrial disease and motor neuron degeneration [2]. Our KI mouse model, generated by homologous recombination, reflects the human context because the heterozygous deleterious allele is constitutively expressed in all murine cells. The mice are viable and healthy at birth. The first clinical signs start at 3 months when *CHCHD10*$^{S59L/+}$ animals show significantly reduced weight compared to controls. Before 14 months, all KI mice were euthanized for ethical reasons related to severe and rapid weight loss associated with tremors, thus demonstrating the deleterious effect of the

variant p.Ser59Leu in the mouse model. In our original family, all affected individuals carrying the p.Ser59Leu variant presented a typical late-onset mitochondrial myopathy associated with mtDNA deletions [2]. The mouse model mimics the human disease because all KI animals have a myopathy with a deficient activity of all RC complexes, low expression levels of OXPHOS proteins, mtDNA instability and altered mitochondria ultrastructure by electron microscopy at end stage. Patients had other symptoms, different from one individual to another, including signs of motor neuron degeneration. Between 6 and 12 months, the *CHCHD10*$^{S59L/+}$ mice present a rapid weight loss that is observed in ALS but the animals are not paralyzed like in murine models of MND expressing mutations in *SOD1* or in other ALS genes (for review, see Philips and Rothstein [31]). However, we found morphological abnormalities of NMJs with moderate but significant neuron loss in the spinal cord of the mutant animals at end stage. The level of neuron loss (15.17%) is consistent with the absence of paralysis in *CHCHD10*$^{S59L/+}$ mice which appears from 30 to 50% loss of motor neurons in SOD1 mice [25]. We also observed TDP-43 pathology in spinal neurons at this stage, thus confirming the interest of *CHCHD10*$^{S59L/+}$ mice as an ALS model. Importantly, we showed that the expression of the p.Ser59Leu allele did sensitize motor neuron cell lines, as well as iPSC-derived human motor neurons, to apoptosis. Altogether these results demonstrate that the expression of the p.Ser59Leu variant favors motor neuron degeneration and that OXPHOS deficiency can be at the origin of MND also in mouse.

ALS is a fatal disease leading to motor neuron death and progressive paralysis with muscle atrophy. Growing evidence suggests that disease may begin at the distal axon proceeding in a "dying-back" pattern in which NMJ degeneration plays a key role in the progression of pathological events [8, 11, 27, 28, 33]. Defects in expression of AChRs in skeletal muscle are found in ALS, even in the absence of motor neuron abnormalities, and the number and localization of AChR patches are involved in the stability of NMJ [5, 29]. The fragmentation of the post-synaptic motor end plate is correlated with a decline in the efficacy of neuromuscular transmission at NMJs [42]. In *CHCHD10*$^{S59L/+}$ animals, we found both abnormalities of AChRs localization and hyperfragmentation of the motor end plate at end stage showing a degeneration of post-synaptic part of the NMJ. These abnormalities, associated with a significant decrease in the number of motor neurons and a TDP-43 proteinopathy in the lumbar spinal cord, showed that mutant mice present signs of MND around 1 year of age.

Axonal and NMJ degeneration is a complex and evolving sequence of events. It has been proposed that the muscle itself may initiate the pathology that then would lead to NMJ destruction, motor neuron degeneration and death [5, 10, 12]. We found OXPHOS deficiency in muscle of *CHCHD10*$^{S59L/+}$ animals at 3 months of age in the absence of neuronal loss in spinal cord. From 3 months, mice also showed lower body mass compared with controls despite normal caloric intake (not shown) suggesting the involvement of a hypercatabolic process. Chronic hypercatabolism is found both in patients and mouse models of ALS, while its origin still remains unsolved [9, 12, 13]. In *CHCHD10*$^{S59L/+}$ animals, it is likely related to muscle energy deficiency. Reduced RC activity has been described in both patients and models of ALS and may significantly contribute to pathogenesis (for review see Cozzolino et al. [7] and Smith et al. [37]). Decreased ATP production in the subsarcolemmal mitochondria located near the NMJ may impair both neurotransmission and vesicular recycling. We found that CHCHD10 is highly expressed in the subsarcolemmal pool of mitochondria closed to the NMJ and that this expression is dysregulated in mutant animals presenting fragmented motor end plate. We previously showed that CHCHD10 is enriched at mitochondrial cristae junctions and that the *CHCHD10* p.Ser59Leu mutation promotes loss of mitochondrial cristae junctions in patient fibroblasts [2, 15]. The CHCHD10 concentration within mitochondria of the post-synaptic region probably reflects an important role in synaptic transmission between motor neuron and muscle fiber. The effects of the p.Ser59Leu mutation on the internal membrane structure associated with OXPHOS deficiency within mitochondria at motor end plate are likely a determining factor of NMD-associated muscle pathology. Around 1 year of age, *CHCHD10*$^{S59L/+}$ mice presented a mitochondrial myopathy with morphological abnormalities of the NMJs and a moderate but significant loss of motor neurons in spinal cord. At this stage, we did not find scattered or grouped atrophic muscle fibers, a characteristic consequence of denervation in muscle from ALS patients. This result confirms that muscle damage was not secondary to MND in our model. Indeed, the loss of motor neurons was likely not pronounced enough to lead to denervation signs in the muscle of *CHCHD10*$^{S59L/+}$ mice at that stage. We also observed that the severity of mitochondrial dysfunction in muscle was much greater than the one observed in spinal cord of mutant animals. Last, we found abnormal expression of CHCHD10 in KI mice, with accumulation areas as patches, near the NMJs including those that were morphologically normal, suggesting that the deleterious effects of the p.Ser59Leu allele target the muscle prior to the NMJ. Altogether, our results are consistent with a key role of muscle in MND associated with *CHCHD10* mutations. However, the p.Ser59Leu mutation can also have a cell-autonomous deleterious effect on motor neurons, without a first hit at the muscle and be responsible for two parallel degenerative phenomenons in muscle and in motor neuron. The generation of mice selectively expressing the p.Ser59Leu mutation in motor neurons or in muscle will

be needed to determine whether mitochondrial deficiency in muscle is essential to the disease.

At the end stage, *CHCHD10*$^{S59L/+}$ mice show early signs of motor neuron degeneration that do not explain their sudden decompensation that requires euthanasia. This worsening is related to a severe cardiomyopathy in mutant animals. *CHCHD10*$^{S59L/+}$ mice present cardiomyopathy with a clearly impaired systolic function. We also observed conduction defects, which are presumably secondary to the involvement of the cardiac muscle. Although hearts were macroscopically normal, microscopic examination revealed signs of cardiomyocyte degeneration linked to severe OXPHOS deficiency with COX-negative fibers, multiple defect of RC complexes activity and a quite important loss of mtDNA molecules. Ultrastructural analysis also revealed a complete disorganization of myofibers. Heart disease was not present in patients bearing the p.Ser59Leu mutation in *CHCHD10* [2]. However, cardiac involvement is recognized in about a third of children and up to 80% of adults with OXPHOS disorders [23, 45]. Furthermore, the p.Gly58Arg variant of *CHCHD10* has been identified in a family presenting cardiomyopathy and mitochondrial myopathy with autosomal dominant inheritance [36] (Joanna Poulton, personal communication), indicating that *CHCHD10*$^{S59L/+}$ mice may also be an interesting model for cardiac involvement linked to *CHCHD10* mutations in human. OXPHOS deficiency was already present in the heart of the mutant animals at 3 months of age with a deficiency of complexes II and IV activities, decreased expression levels of RC proteins and mtDNA depletion [suppl. Figure 5 (Online Resource 7)]. These results, associated with the findings from mice at 3 months of age, show that deleterious effects of the p.Ser59Leu mutation preferentially target cardiac and peripheral muscles.

Accumulating evidence suggests that mitophagy dysregulation can induce cardiomyocyte death and cardiomyopathy (for review, see Tong and Sadoshima [39]). Several arguments, including decreased citrate synthase activity, vacuolization of cardiomyocytes and dramatic loss of mtDNA copies in the heart of mutant mice at end stage, were evocative of altered autophagy/mitophagy. Increased LC3-II expression level revealed that general autophagy is enhanced and the numerous autophagosomes, containing only mitochondria, observed by electron microscopic analyses of heart sections support the increase of mitophagy in cardiomyocytes from *CHCHD10*$^{S59L/+}$ mice at end stage. It has been shown that chloroquine, an autophagy inhibitor, has therapeutic effects on left ventricular function in diabetic mice that present cardiomyopathy linked to enhanced autophagy [46]. The severity of heart disease in *CHCHD10*$^{S59L/+}$ mice prevented us from following the evolution of MND. Treating mice with autophagy inhibitors may be able to increase their lifespan and allow studying later events leading to the death of motor neurons.

In conclusion, we generated novel models that allowed to confirm that mitochondrial defect can trigger MND and that the expression of the p.Ser59Leu variant in *CHCHD10* sensitizes motor neurons to stress-induced death. In a back-to-back publication, Giovanni Manfredi's team describes a similar phenotype in KI mice carrying the same mutation in *CHCHD10*, generated with CRISPR/Cas9 system. Both manuscripts highlight complementary aspects of *CHCHD10*-related disease: (1) the role of the aggregates of CHCHD10 and its paralogous CHCHD2 in the mitochondrial stress response leading to aberrant organelle function and, (2) the dissection of the kinetics of events leading to motor neuron death. The kinetics of pathological events in our mouse model and the CHCHD10 expression patterns in both WT and mutant mice are in favor with a key role for muscle in *CHCHD10*-associated MND.

Acknowledgements We thank our colleagues from Genetic Engineering and Mouse Transgenesis department at service unit CIPHE (Centre d'Immunophénomique, Aix Marseille Université, INSERM, CNRS, Phenomin, Marseille, France) and mainly Frederic Fiore who provided expertise and know-how and perform the generation of the *CHCHD10*$^{S59L/+}$ mice that greatly assisted our project. We also thank our colleagues, including Benoit Petit-Demoulière, Ghina Bou-About, Hamid Meziane, Hugues Jacobs, Marie-France Champy, Patrick Reilly, Tania Sorg and Yann Herault from Phenomin (Institut Clinique de la souris, 1 rue Laurent Fries, 67404 ILLKIRCH cedex 2—CNRS, UMR7104, Illkirch, France—INSERM, U964, Illkirch, France—Université de Strasbourg, France) for their help in phenotyping mice. We gratefully acknowledge the IRCAN's Molecular and Cellular Core Imaging (PICMI) facility, supported financially by FEDER, Conseil régional Provence Alpes-Côte d'Azur, Conseil Départemental 06, Cancéropôle PACA, Gis Ibisa and Inserm, the IRCAN's Animal core facility, supported by Région Provence Alpes-Côte d'Azur and Inserm, the IRCAN's Histology core facility, supported by Région Provence Alpes-Côte d'Azur and Université de Nice Sophia-Antipolis, the Centre Méditerranéen de Médecine Moléculaire (C3 M) imaging facility, the University's CCMA Electron Microscopy facility supported by Université de Nice Sophia-Antipolis, Région Provence Alpes-Côte d'Azur, Conseil Départemental 06, and Gis Ibisa and, the ICM CELIS-iPS internal platform. We also thank Dr Luisa Villa and Dr Pamela Moceri for their help in interpreting muscle and cardiac results, respectively, and Sandra Foustoul and Alyssia Mari for technical help.

Author contributions ECG and SBa designed, performed experiments and analyzed data on mouse models, and contributed to the main text. BMH designed, performed experiments and analyzed data on cell models (NSC34 and iPSCs-derived motor neurons), and contributed to the main text. KF designed, performed experiments and analyzed data on respiratory chain experiments. SL-G performed electron microscopy experiments. JN, AM-C, FL, BR, GA and CC performed and analyzed experiments on mouse models. SBi generated iPSC. CL-O and DB provided the motor neuron differentiation protocol and advices on the iPSC daily culture and motor neuron differentiation. DB provides advices and helped in data interpretation on iPSC-derived motor neuron experiments and contributed to the main text. AC provided technical advices for motor neurons staining and count. FM helped with the interpretation of metabolic data. SBo and CL provided advices for the NMJ and motor neurons analyses and helped in data interpretation.

J-ER designed and analyzed data on cell models and contributed to the main text. VP-F designed, supervised the project and drafted the manuscript. All the authors read and approved the final submission.

Funding This work was made possible by Grants to VP-F from the ANR (Agence Nationale de la Recherche) ANR-16-CE16-0024-01, from the AFM-Téléthon (Association Française contre les Myopathies) #20947 and from the Fondation Maladies Rares. The research leading to the iPSC results has received funding from the program "Investissements d'avenir" ANR-11-INBS-0011-NeurATRIS: Translational Research Infrastructure for Biotherapies in Neurosciences". ECG and BMH are postdoctoral fellows supported by ANR-16-CE16-0024-01. CL-O is a Ph.D. fellow supported by ANR-10-LABX-73.

Compliance with ethical standards

Conflict of interest No conflict of interest.

References

1. Auranen M, Ylikallio E, Shcherbii M, Paetau A, Kiuru-Enari S, Toppila JP et al (2015) CHCHD10 variant p.(Gly66Val) causes axonal Charcot–Marie–Tooth disease. Neurol Genet 1:e1. https://doi.org/10.1212/nxg.0000000000000003
2. Bannwarth S, Ait-El-Mkadem S, Chaussenot A, Genin EC, Lacas-Gervais S, Fragaki K et al (2014) A mitochondrial origin for frontotemporal dementia and amyotrophic lateral sclerosis through CHCHD10 involvement. Brain J Neurol 137:2329–2345. https://doi.org/10.1093/brain/awu138
3. Bannwarth S, Berg-Alonso L, Augé G, Fragaki K, Kolesar JE, Lespinasse F et al (2016) Inactivation of Pif1 helicase causes a mitochondrial myopathy in mice. Mitochondrion 30:126–137. https://doi.org/10.1016/j.mito.2016.02.005
4. Blasco H, Mavel S, Corcia P, Gordon PH (2014) The glutamate hypothesis in ALS: pathophysiology and drug development. Curr Med Chem 21:3551–3575
5. Bloch-Gallego E (2015) Mechanisms controlling neuromuscular junction stability. Cell Mol Life Sci 72:1029–1043. https://doi.org/10.1007/s00018-014-1768-z
6. Bradford MM (1976) A rapid and sensitive method for the quantitation of microgram quantities of protein utilizing the principle of protein-dye binding. Anal Biochem 72:248–254. https://doi.org/10.1016/0003-2697(76)90527-3
7. Cozzolino M, Rossi S, Mirra A, Carrì MT (2015) Mitochondrial dynamism and the pathogenesis of amyotrophic lateral sclerosis. Front Cell Neurosci 9:31. https://doi.org/10.3389/fncel.2015.00031
8. Dadon-Nachum M, Melamed E, Offen D (2011) The "Dying-Back" phenomenon of motor neurons in ALS. J Mol Neurosci 43:470–477. https://doi.org/10.1007/s12031-010-9467-1
9. Desport JC, Preux PM, Magy L, Boirie Y, Vallat JM, Beaufrère B et al (2001) Factors correlated with hypermetabolism in patients with amyotrophic lateral sclerosis. Am J Clin Nutr 74:328–334. https://doi.org/10.1093/ajcn/74.3.328
10. Dobrowolny G, Aucello M, Rizzuto E, Beccafico S, Mammucari C, Bonconpagni S et al (2008) Skeletal muscle is a primary target of SOD1G93A-mediated toxicity. Cell Metab 8:425–436. https://doi.org/10.1016/j.cmet.2008.09.002
11. Dupuis L, Gonzalez de Aguilar J-L, Echaniz-Laguna A, Eschbach J, Rene F, Oudart H et al (2009) Muscle mitochondrial uncoupling dismantles neuromuscular junction and triggers distal degeneration of motor neurons. PLoS One 4:e5390. https://doi.org/10.1371/journal.pone.0005390
12. Dupuis L, Gonzalez de Aguilar J-L, Oudart H, de Tapia M, Barbeito L, Loeffler J-P (2004) Mitochondria in amyotrophic lateral sclerosis: a trigger and a target. Neurodegener Dis 1:245–254. https://doi.org/10.1159/000085063
13. Dupuis L, Pradat P-F, Ludolph AC, Loeffler J-P (2011) Energy metabolism in amyotrophic lateral sclerosis. Lancet Neurol 10:75–82. https://doi.org/10.1016/S1474-4422(10)70224-6
14. Genin EC, Bannwarth S, Lespinasse F, Ortega-Vila B, Fragaki K, Itoh K et al (2018) Loss of MICOS complex integrity and mitochondrial damage, but not TDP-43 mitochondrial localisation, are likely associated with severity of CHCHD10-related diseases. Neurobiol Dis 119:159–171. https://doi.org/10.1016/j.nbd.2018.07.027
15. Genin EC, Plutino M, Bannwarth S, Villa E, Cisneros-Barroso E, Roy M et al (2016) CHCHD10 mutations promote loss of mitochondrial cristae junctions with impaired mitochondrial genome maintenance and inhibition of apoptosis. EMBO Mol Med 8:58–72. https://doi.org/10.15252/emmm.201505496
16. Gorman GS, McFarland R, Stewart J, Feeney C, Turnbull DM (2018) Mitochondrial donation: from test tube to clinic. Lancet 392:1191–1192. https://doi.org/10.1016/S0140-6736(18)31868-3
17. Guo W, Naujock M, Fumagalli L, Vandoorne T, Baatsen P, Boon R et al (2017) HDAC6 inhibition reverses axonal transport defects in motor neurons derived from FUS-ALS patients. Nat Commun. https://doi.org/10.1038/s41467-017-00911-y
18. Hell K (2008) The Erv1–Mia40 disulfide relay system in the intermembrane space of mitochondria. Biochim Biophys Acta BBA Mol Cell Res 1783:601–609. https://doi.org/10.1016/j.bbamcr.2007.12.005
19. Huang ML-H, Sivagurunathan S, Ting S, Jansson PJ, Austin CJD, Kelly M et al (2013) Molecular and functional alterations in a mouse cardiac model of friedreich ataxia. Am J Pathol 183:745–757. https://doi.org/10.1016/j.ajpath.2013.05.032
20. Johnson JO, Glynn SM, Gibbs JR, Nalls MA, Sabatelli M, Restagno G, Drory VE et al (2014) Mutations in the CHCHD10 gene are a common cause of familial amyotrophic lateral sclerosis. Brain J Neurol 137:e311. https://doi.org/10.1093/brain/awu265
21. Jones RA, Reich CD, Dissanayake KN, Kristmundsdottir F, Findlater GS, Ribchester RR et al (2016) NMJ-morph reveals principal components of synaptic morphology influencing structure–function relationships at the neuromuscular junction. Open Biol 6:160240. https://doi.org/10.1098/rsob.160240
22. Lehmer C, Schludi MH, Ransom L, Greiling J, Junghänel M, Exner N et al (2018) A novel CHCHD10 mutation implicates a Mia40-dependent mitochondrial import deficit in ALS. EMBO Mol Med 10:e8558. https://doi.org/10.15252/emmm.201708558
23. Limongelli G, Tome-Esteban M, Dejthevaporn C, Rahman S, Hanna MG, Elliott PM (2010) Prevalence and natural history of heart disease in adults with primary mitochondrial respiratory chain disease. Eur J Heart Fail 12:114–121. https://doi.org/10.1093/eurjhf/hfp186
24. Maury Y, Côme J, Piskorowski RA, Salah-Mohellibi N, Chevaleyre V, Peschanski M et al (2015) Combinatorial analysis of developmental cues efficiently converts human pluripotent stem cells into multiple neuronal subtypes. Nat Biotechnol 33:89–96. https://doi.org/10.1038/nbt.3049
25. Mesci P, Zaïdi S, Lobsiger CS, Millecamps S, Escartin C, Seilhean D et al (2015) System xC—is a mediator of microglial function and its deletion slows symptoms in amyotrophic lateral sclerosis mice. Brain 138:53–68. https://doi.org/10.1093/brain/awu312
26. Müller K, Andersen PM, Hübers A, Marroquin N, Volk AE, Danzer KM et al (2014) Two novel mutations in conserved codons indicate that CHCHD10 is a gene associated with motor neuron disease. Brain J Neurol 137:e309. https://doi.org/10.1093/brain/awu227

27. Musarò A, McCullagh K, Paul A, Houghton L, Dobrowolny G, Molinaro M et al (2001) Localized Igf-1 transgene expression sustains hypertrophy and regeneration in senescent skeletal muscle. Nat Genet 27:195–200. https://doi.org/10.1038/84839
28. Palma E, Inghilleri M, Conti L, Deflorio C, Frasca V, Manteca A et al (2011) Physiological characterization of human muscle acetylcholine receptors from ALS patients. Proc Natl Acad Sci 108:20184–20188. https://doi.org/10.1073/pnas.1117975108
29. Palma E, Reyes-Ruiz JM, Lopergolo D, Roseti C, Bertollini C, Ruffolo G et al (2016) Acetylcholine receptors from human muscle as pharmacological targets for ALS therapy. Proc Natl Acad Sci 113:3060–3065. https://doi.org/10.1073/pnas.1600251113
30. Penttilä S, Jokela M, Bouquin H, Saukkonen AM, Toivanen J, Udd B (2015) Late onset spinal motor neuronopathy is caused by mutation in CHCHD10. Ann Neurol 77:163–172. https://doi.org/10.1002/ana.24319
31. Philips T, Rothstein JD (2015) Rodent models of amyotrophic lateral sclerosis: rodent models of ALS. Curr Protoc Pharmacol 69:5.67.1–5.67.21. https://doi.org/10.1002/0471141755.ph0567s69
32. Raff MC (2002) Axonal self-destruction and neurodegeneration. Science 296:868–871. https://doi.org/10.1126/science.1068613
33. Rocha MC, Pousinha PA, Correia AM, Sebastião AM, Ribeiro JA (2013) Early Changes of neuromuscular transmission in the SOD1(G93A) mice model of ALS start long before motor symptoms onset. PLoS One 8:e73846. https://doi.org/10.1371/journal.pone.0073846
34. Ronchi D, Riboldi G, Del Bo R, Ticozzi N, Scarlato M, Galimberti D et al (2015) CHCHD10 mutations in Italian patients with sporadic amyotrophic lateral sclerosis. Brain J Neurol 138:e372. https://doi.org/10.1093/brain/awu384
35. Rustin P, Chretien D, Bourgeron T, Gérard B, Rötig A, Saudubray JM et al (1994) Biochemical and molecular investigations in respiratory chain deficiencies. Clin Chim Acta Int J Clin Chem 228:35–51
36. Salmon M, Esiri M, Ruderman N (1971) Myopathic disorder associated with mitochondrial abnormalities, hyperglycaemia, and hyperketonaemia. Lancet 298:290–293. https://doi.org/10.1016/S0140-6736(71)91335-3
37. Smith EF, Shaw PJ, De Vos KJ (2017) The role of mitochondria in amyotrophic lateral sclerosis. Neurosci Lett. https://doi.org/10.1016/j.neulet.2017.06.052
38. The International Stem Cell Banking Initiative (2009) Consensus guidance for banking and supply of human embryonic stem cell lines for research purposes. Stem Cell Rev Rep 5:301–314. https://doi.org/10.1007/s12015-009-9085-x
39. Tong M, Sadoshima J (2016) Mitochondrial autophagy in cardiomyopathy. Curr Opin Genet Dev 38:8–15. https://doi.org/10.1016/j.gde.2016.02.006
40. Van Den Bosch L, Van Damme P, Bogaert E, Robberecht W (2006) The role of excitotoxicity in the pathogenesis of amyotrophic lateral sclerosis. Biochim Biophys Acta BBA Mol Basis Dis 1762:1068–1082. https://doi.org/10.1016/j.bbadis.2006.05.002
41. Villa E, Proïcs E, Rubio-Patiño C, Obba S, Zunino B, Bossowski JP et al (2017) Parkin-independent mitophagy controls chemotherapeutic response in cancer cells. Cell Rep 20:2846–2859. https://doi.org/10.1016/j.celrep.2017.08.087
42. Willadt S, Nash M, Slater CR (2016) Age-related fragmentation of the motor endplate is not associated with impaired neuromuscular transmission in the mouse diaphragm. Sci Rep. https://doi.org/10.1038/srep24849
43. Wishart TM, Parson SH, Gillingwater TH (2006) Synaptic vulnerability in neurodegenerative disease. J Neuropathol Exp Neurol 65:733–739. https://doi.org/10.1097/01.jnen.0000228202.35163.c4
44. Woo J-AA, Liu T, Trotter C, Fang CC, De Narvaez E, LePochat P et al (2017) Loss of function CHCHD10 mutations in cytoplasmic TDP-43 accumulation and synaptic integrity. Nat Commun 8:15558. https://doi.org/10.1038/ncomms15558
45. Yaplito-Lee J, Weintraub R, Jamsen K, Chow CW, Thorburn DR, Boneh A (2007) Cardiac manifestations in oxidative phosphorylation disorders of childhood. J Pediatr 150:407–411. https://doi.org/10.1016/j.jpeds.2006.12.047
46. Yuan X, Xiao Y-C, Zhang G-P, Hou N, Wu X-Q, Chen W-L et al (2016) Chloroquine improves left ventricle diastolic function in streptozotocin-induced diabetic mice. Drug Des Dev Ther 10:2729–2737. https://doi.org/10.2147/DDDT.S111253

Affiliations

Emmanuelle C. Genin[1] · Blandine Madji Hounoum[2] · Sylvie Bannwarth[1] · Konstantina Fragaki[1] · Sandra Lacas-Gervais[3] · Alessandra Mauri-Crouzet[1] · Françoise Lespinasse[1] · Julien Neveu[1] · Baptiste Ropert[1] · Gaelle Augé[1] · Charlotte Cochaud[1] · Cynthia Lefebvre-Omar[4] · Stéphanie Bigou[4] · Aude Chiot[4] · Fanny Mochel[4,5] · Séverine Boillée[4] · Christian S. Lobsiger[4] · Delphine Bohl[4] · Jean-Ehrland Ricci[2] · Véronique Paquis-Flucklinger[1]

[1] Inserm U1081, CNRS UMR7284, IRCAN, CHU de Nice, Medicine School, Université Côte d'Azur, 28 av de Valombrose, 06107 Nice Cedex 2, France

[2] Inserm U1065, C3M, Université Côte d'Azur, Nice, France

[3] Centre Commun de Microscopie Appliquée, Université Côte d'Azur, Nice, France

[4] Institut du Cerveau et de la Moelle Epinière, ICM, Inserm, U1127, CNRS UMR7225, Sorbonne Universités, 75013 Paris, France

[5] Department of Genetics and Reference Centre for Adult Neurometabolic Diseases, AP-HP, La Pitié-Salpêtriere University Hospital, Paris, France